ELEMENTA
Science of the Anthropocene

Webster, MA, et al. 2022. Spatiotemporal evolution of melt ponds on Arctic sea ice: MOSAiC observations and model results. *Elem Sci Anth*, 10: 1. DOI: https://doi.org/10.1525/elementa.2021.000072

RESEARCH ARTICLE

Spatiotemporal evolution of melt ponds on Arctic sea ice: MOSAiC observations and model results

Melinda A. Webster[1,*], Marika Holland[2], Nicholas C. Wright[3], Stefan Hendricks[4], Nils Hutter[4], Polona Itkin[5], Bonnie Light[6], Felix Linhardt[7], Donald K. Perovich[8], Ian A. Raphael[8], Madison M. Smith[6], Luisa von Albedyll[4], and Jinlun Zhang[6]

Melt ponds on sea ice play an important role in the Arctic climate system. Their presence alters the partitioning of solar radiation: decreasing reflection, increasing absorption and transmission to the ice and ocean, and enhancing melt. The spatiotemporal properties of melt ponds thus modify ice albedo feedbacks and the mass balance of Arctic sea ice. The Multidisciplinary drifting Observatory for the Study of Arctic Climate (MOSAiC) expedition presented a valuable opportunity to investigate the seasonal evolution of melt ponds through a rich array of atmosphere-ice-ocean measurements across spatial and temporal scales. In this study, we characterize the seasonal behavior and variability in the snow, surface scattering layer, and melt ponds from spring melt to autumn freeze-up using in situ surveys and auxiliary observations. We compare the results to satellite retrievals and output from two models: the Community Earth System Model (CESM2) and the Marginal Ice Zone Modeling and Assimilation System (MIZMAS). During the melt season, the maximum pond coverage and depth were 21% and 22 $\pm$ 13 cm, respectively, with distribution and depth corresponding to surface roughness and ice thickness. Compared to observations, both models overestimate melt pond coverage in summer, with maximum values of approximately 41% (MIZMAS) and 51% (CESM2). This overestimation has important implications for accurately simulating albedo feedbacks. During the observed freeze-up, weather events, including rain on snow, caused high-frequency variability in snow depth, while pond coverage and depth remained relatively constant until continuous freezing ensued. Both models accurately simulate the abrupt cessation of melt ponds during freeze-up, but the dates of freeze-up differ. MIZMAS accurately simulates the observed date of freeze-up, while CESM2 simulates freeze-up one-to-two weeks earlier. This work demonstrates areas that warrant future observation-model synthesis for improving the representation of sea-ice processes and properties, which can aid accurate simulations of albedo feedbacks in a warming climate.

Keywords: Sea ice, Arctic, Melt ponds, Snow

1. Introduction

One of the most distinguishing characteristics of melting Arctic sea ice is the presence of melt ponds. Melt ponds have drastic effects on the partitioning of sunlight reaching the sea-ice surface. Relative to bare sea ice, melt ponds decrease the amount of reflected solar radiation and increase the amount of absorbed and transmitted solar radiation (Perovich et al., 2002a; Perovich and Polashenski, 2012). These effects enhance the warming of the upper ocean, sea-ice melt, and the amount of photosynthetically active radiation available for primary productivity within and beneath the ice cover (Light et al., 2008; Light et al., 2015; Nicolaus et al., 2012; Katlein et al., 2019). Melt ponds initially form through the pooling of freshwater from melting snow into surface depressions (Petrich et al., 2012). The amount of available meltwater from snow and ice, surface roughness, and ice permeability control the timing, location, and extent of melt pond formation (Eicken et al., 2002; Eicken et al., 2004; Polashenski et al., 2012; Webster et al., 2015). Although melt ponds play a critical role in the albedo and mass balance of Arctic sea ice (Flocco et al., 2012; Holland et al., 2012; Hunke et al.,

[1] Geophysical Institute, University of Alaska Fairbanks, Fairbanks, AK, USA
[2] National Center for Atmospheric Research, Boulder, CO, USA
[3] Cold Regions Research and Engineering Laboratory, Hanover, NH, USA
[4] Helmholtz Centre for Polar and Marine Research, Alfred Wegener Institute, Bremerhaven, Germany
[5] Norwegian Polar Institute, Tromsø, Norway
[6] Polar Science Center, Applied Physics Laboratory, University of Washington, Seattle, WA, USA
[7] Institut für Geographie, Christian-Albrechts-Universität zu Kiel, Kiel, Germany
[8] Thayer School of Engineering, Dartmouth College, Hanover, NH, USA

* Corresponding author:
Email: mwebster3@alaska.edu

2013; Schröder et al., 2014), several knowledge gaps remain about melt pond evolution across the Arctic. These knowledge gaps include the:

1. seasonal evolution of melt pond coverage over different sea-ice conditions, and
2. spatio-temporal changes in pond depth and coverage.

For (1), large differences in the timing and extent of pond coverage have been observed between first-year and multiyear ice types at local scales using in situ and high-resolution satellite imagery (Fetterer and Untersteiner, 1998; Eicken et al., 2004; Webster et al., 2015; 2022). However, these differences become ambiguous at regional scales (Rösel et al., 2012; Buckley et al., 2020; Wright et al., 2020). This ambiguity may be related to biases and uncertainties in coarse-resolution satellite retrievals (Wright and Polashenski, 2020) and/or to the effects of heterogeneous sea-ice properties on pond coverage at larger spatial scales, including ice permeability and surface roughness. Model simulations of long-term changes in melt pond coverage show even larger discrepancies (Hunke et al., 2013; Zhang et al., 2018), which likely stem from limited observations and difficulties in parameterizing melt pond processes related to (1) and (2) above.

To date, several model parameterizations either implicitly or explicitly represent the production and retention of surface meltwater, pond area and depth evolution across the ice thickness distribution, and/or vertical and lateral pond drainage. Even so, the sophistication of melt pond parameterizations varies greatly by model (Lüthje et al., 2006; Flocco and Feltham, 2007; Scott and Feltham, 2010; Hunke et al., 2013; Skyllingstad et al., 2015; Popovic and Abbot, 2017; Zhang et al., 2018). Some parameterizations distribute melt ponds sequentially by increasing ice thickness within the sub-grid scale ice thickness distribution (Flocco et al., 2010), while others distribute melt ponds on the level ice portion of the sub-grid scale ice thickness distribution (Hunke et al., 2013). The effects of different pond parameterizations on simulated sea ice also varies. In some model simulations, sea ice is highly sensitive to melt pond drainage parameters (Turner and Hunke, 2015), while in others, sea ice is strongly affected by the sequence in which ponds form across ice thickness categories (Flocco et al., 2010). Melt pond processes are just one example of incomplete model physics that may contribute to the discrepancies in the rate of Arctic sea-ice loss between climate models (Massonnet et al., 2012; Stroeve et al., 2012), which underscores the need for process-oriented observations to advance knowledge of (1) and (2).

This study provides new information on melt pond processes, which may aid the enhancement of model parameterizations involving melt pond evolution and give insight into the mechanisms that influence pond coverage across multiple spatial scales. With the MOSAiC expedition (Shupe et al., 2020), a valuable opportunity arose to document melt pond evolution in situ from spring melt to autumn freeze-up. Melt ponds were measured at nested spatial scales for both assessing the realism of sea ice and climate models and validating airborne and satellite retrievals of melt pond properties in large-scale monitoring. In this work, we present findings on the summer evolution of surface conditions on the MOSAiC expedition from surface-based surveys in May 2020 through September 2020. We characterize the spring–summer transition, from a snow-covered ice surface to an icescape covered in melt ponds and bare ice with a surface scattering layer (SSL), and the summer–autumn transition from open ponds to a frozen state with a newly-formed snow cover.

The MOSAiC observations are compared with those derived from sub-meter resolution airborne and satellite imagery from previous field campaigns to pinpoint geophysical sources of similarities and discrepancies. The results are used further with models to assess the key properties relevant for accurately simulating the seasonal evolution of surface conditions of Arctic sea ice. The objectives of this paper are three-fold: (1) to give a detailed record of a legacy dataset designed for aiding future development of model parameterizations and remote sensing retrievals of sea-ice properties, (2) to demonstrate the use and limitations of comparing in situ observations of melt ponds with model output, and (3) to identify areas of future observation-model synthesis for accurately simulating albedo feedbacks in the Arctic climate system.

2. Data and methods

2.1. What is a melt pond?

Here, we define the nomenclature of snow/SSL, subnivean ponds, and melt ponds used in this analysis so that the results may be more easily compared to other studies and more readily interpreted. The SSL is an optical property of melting sea ice and can be described as deteriorated, granular melting ice, somewhat similar in appearance to large-grained melting snow (Light et al., 2008; 2015). The snow/SSL category combines measurements of both snow and the SSL since different parts of the survey route transitioned to an SSL at different times, with some snow persisting throughout the melt season. Furthermore, the magnaprobe, the instrument used to measure snow depth, penetrates snow and the SSL equally in melting conditions, which makes separating the measurements unfeasible. We use "snow" and "SSL" interchangeably except where noted.

A subnivean pond is defined here as a snow-covered surface with pooled pond water at the base of the snowpack (**Figure 1a**). This condition was often observed in surface depressions which typically formed into ponds as surface melt progressed. Given that a subnivean pond often appears as snow or bare sea ice to satellite sensors in the visible range and its albedo is treated as melting snow in some climate models (e.g., Hunke et al., 2015), we combine this surface type with the snow/SSL when computing areal fractions.

Melt ponds are defined as open pools of meltwater under which the sea ice is intact; surveyed ponds may contain ice-free parts (e.g., thaw holes, cracks) and/or drainage channels connecting to leads, but all point-measurements of ponds presented here had ice directly underneath. Ponded areas that melted entirely through

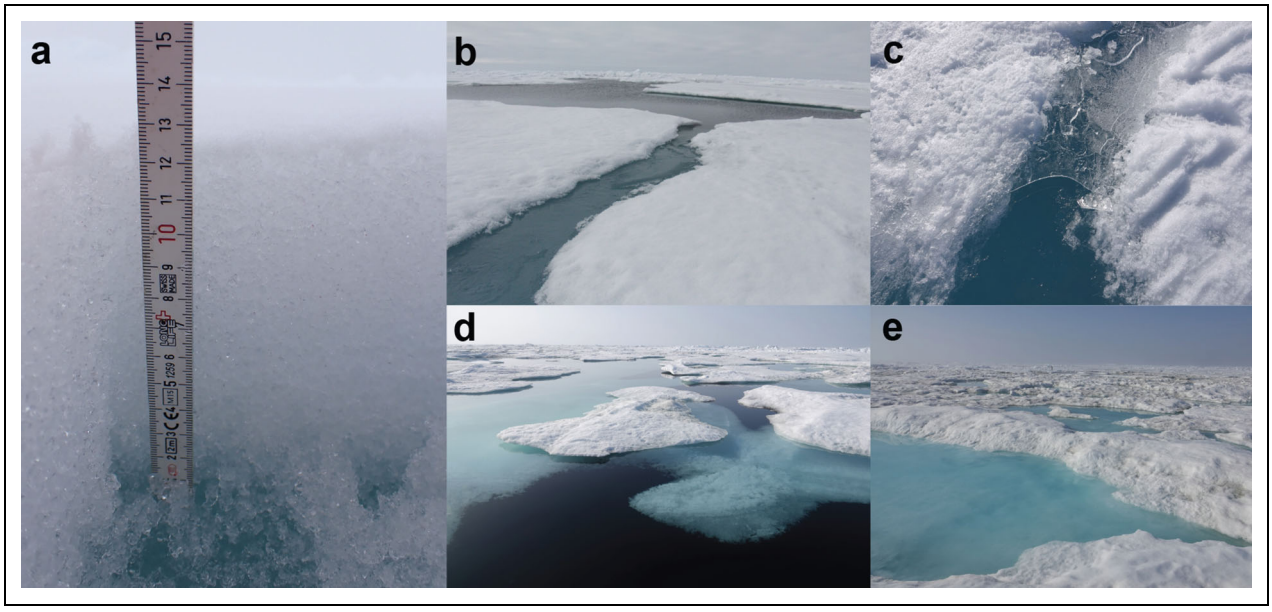

Figure 1. Observed surface features along the transect route. (a) A subnivean pond, a term for the pooled meltwater underneath a snowpack that later becomes a melt pond. (b) Active lateral drainage from a melt pond on first-year ice into a lead on July 5, 2020. The drainage channel in the foreground was about 0.5 m wide. (c) An ice lid approximately 3-mm thick on a pond connected to a lateral drainage channel on June 30, 2020. The lateral drainage channel was about 0.15 m wide. (d) Small portions of the survey route on July 25, 2020 were no longer passable due to ponded ice melting completely, becoming open water. Such open water occurred mostly on level first-year ice. (e) Advanced stages of ponding on hummocky second-year ice on July 26, 2020. DOI: https://doi.org/10.1525/elementa.2021.000072.f1

the ice or had ice bottoms that broke free and floated to the surface were not documented as melt ponds. August–September measurements of ponds include those with ice lids. In cases where the ice lids were sufficiently thick to withstand the weight of surveyors, ponds were classified as refrozen until snow fully masked the surface. Although the magnaprobe measurements showed zero depth for these snow-free pond lids, the zero depth values were excluded in calculations of pond areal fraction and pond depth. Liquid water remained present underneath the majority of pond lids during August–September, which was the duration of the field component at MOSAiC's Central Observatory 3 (CO3).

Pond areal fractions were computed as the pond area divided by the sea ice (non-ponded plus ponded) area. This definition was used for results derived from high-resolution airborne and satellite imagery. The bulk volume of pond water was computed using a fixed area of the floe (931,960 m^2) retrieved from satellite imagery (**Figure 2**), and the mean pond depth and areal pond fraction from the transect data:

$$volume_{pond} = area_{floe} * fraction_{pond} * depth_{pond} \quad (1)$$

2.2. MOSAiC observations

The 2019–2020 MOSAiC expedition was a year-long drift experiment in the central Arctic with the objective of comprehensively documenting the interdependencies of the ecosystem, atmosphere, sea ice, and ocean systems (Nicolaus et al., 2022). The expedition was divided into five legs, during which in situ transect surveys were carried out over different regions and seasons, and, in the case for Legs 1–3, 4, and 5, over different floes, referred to hereafter as central observatories (**Figure 3**; Nicolaus et al., 2022). In this paper, we present transect measurements that were collected during summer melt in June–July 2020 on Central Observatory 2 (CO2) and autumn freeze-up in August–September 2020 on CO3. Snow depth, SSL thickness, and melt pond depth were measured using a magnaprobe, an automated snow depth probe equipped with a GPS logger (Sturm and Holmgren, 2018). Measurements were collected every 1–2 steps, which equated to 1–3-m sampling along repeat transect routes. To accommodate measurements of snow and melt ponds when both were present, the snow basket of the magnaprobe was outfitted with foam on its upper portion to provide buoyancy in melt ponds. The bias associated with this addition was approximately 0.25 cm, which is less than the instrumental uncertainty of 1 cm over sea ice in freezing conditions.

Alongside magnaprobe measurements, a Geophex electromagnetic induction sounding device (GEM-2) was used to derive total (snow + ice) thickness on the transect routes (Hunkeler et al., 2016). The GEM-2 retrieval takes advantage of the large conductivity difference between the ice and ocean. Subtracting the magnaprobe snow depth from the GEM-2 retrieval yields sea-ice thickness. Quicklook data from the GEM-2 are used in Section 3.3.2 for segregating measurements into ice thickness categories. Assuming hydrostatic equilibrium (Table S1),

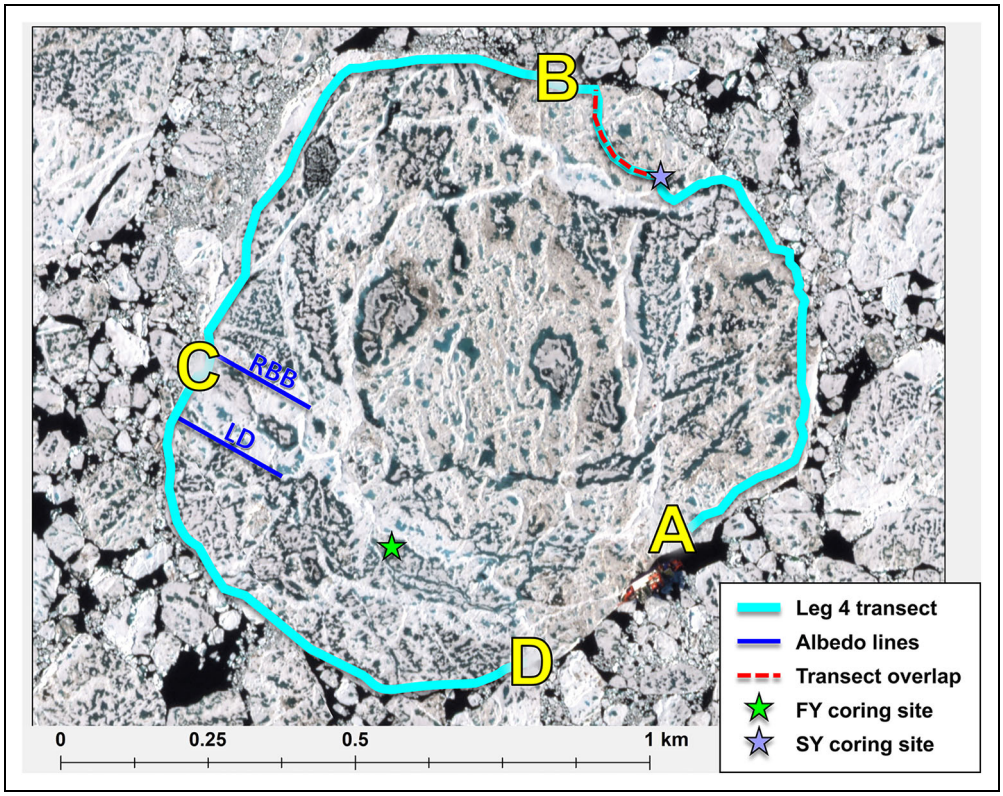

Figure 2. The transect route on Central Observatory 2 (June–July). The yellow letters mark points of relevance: (A) starting point, (B) waypoint called Picnic Ridge, (C) albedo lines (dark blue) called Root Beer Barrel (RBB) and Lemon Drop (LD), and (D) ending point. Transect overlap (dashed red line) refers to the Northern Transect Loop of CO1. The route from A to B covered second-year (SY) ice, while C to D covered mostly first-year (FY) ice. Background image: July 22, 2020, multispectral image from Planet Labs, Inc. A corresponding satellite scene is not available for Central Observatory 3 due to its high latitude location. DOI: https://doi.org/10.1525/elementa.2021.000072.f2

snapshots of the early spring and mid-summer snow, SSL, and sea-ice thickness conditions were produced from the magnaprobe and Quicklook GEM-2 data. We note that further processing of the GEM-2 data is ongoing to achieve high-quality retrievals of sea-ice thickness with low uncertainty. The thickness data set used here is based on empirical evaluation GEM-2 data. In this Quicklook product, the relation of the real part of the 18-kHz frequency with ice thickness is calibrated by drill-hole measurements on the same day. This technique may lead to errors for thicknesses far outside the calibration range (> 10 m). Even so, the retrievals are consistent with other data sources and do not contain outliers, which would bias the results.

In Section 3.3.1, we evaluate melt pond coverage and its relation to pre-melt surface elevations. The surface elevation data were acquired using an airborne laser scanner (ALS), processed to output drift-corrected elevation data above the WGS84 ellipsoid (Hutter et al., 2021), and gridded with a resolution of 0.5 m by 0.5 m. We used airborne measurements from April 8, 2020, weeks before melt onset, to examine the surface roughness characteristics of areas that later became ponded compared to those that remained pond-free. We used the standard deviation in surface elevations as a proxy for surface roughness (Shepard et al., 2001). To spatially align the April 8 airborne elevation measurements to optical satellite images, 10 tie points of matched features were identified manually to reproject the April 8 gridded elevations onto the July optical satellite images. Three masks were created using the July 7 satellite image and surface type retrievals to isolate the ponded areas during near-maximum pond coverage and the bare ice (unponded) areas on CO2 (**Figure 4**). When evaluating surface roughness, we randomly selected the same number of grid points (approximately 435,000) within each surface type to calculate surface roughness. The elevation data set is a pre-release of the final data product that is currently undergoing processing for public release.

2.2.1. CO2: Spring-to-summer melt

Upon arrival to CO2 on June 17, initial surveys were conducted on CO2 and on nearby floes for scientific and operational purposes. The principal transect route was established in segments beginning on June 17 and fully marked on June 29. The CO2 transect route covered approximately 3 km in distance and was surveyed in a counterclockwise pattern along the floe perimeter (**Figure 2**). A 200–300-m portion of the CO2 transect route overlapped with the Northern Transect Loop from CO1 (**Figure 2**), allowing for a comparison of winter and summer conditions. Following sea-ice nomenclature (World Meteorological Organization, 1970), CO2 was predominantly second-year ice (SY), while the last third of the

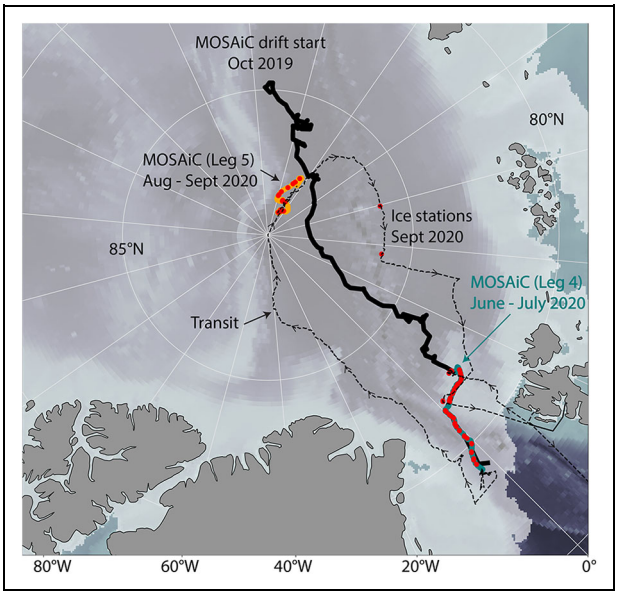

Figure 3. Geographic locations of transect measurements during the summer melt and autumn freeze-up seasons. Melt season measurements were made on Central Observatory 2 during MOSAiC Leg 4 (June–July 2020); freeze-up season measurements, on CO3 during Leg 5 (August–September 2020). The light grey shading is sea-ice extent derived from passive microwave satellite data for June 16, 2020. The red dots indicate locations where transect measurements were made. Ice station measurements were carried out in transit into (June 13, 2020) and out of (September 2020) the ice pack. DOI: https://doi.org/10.1525/elementa.2021.000072.f3

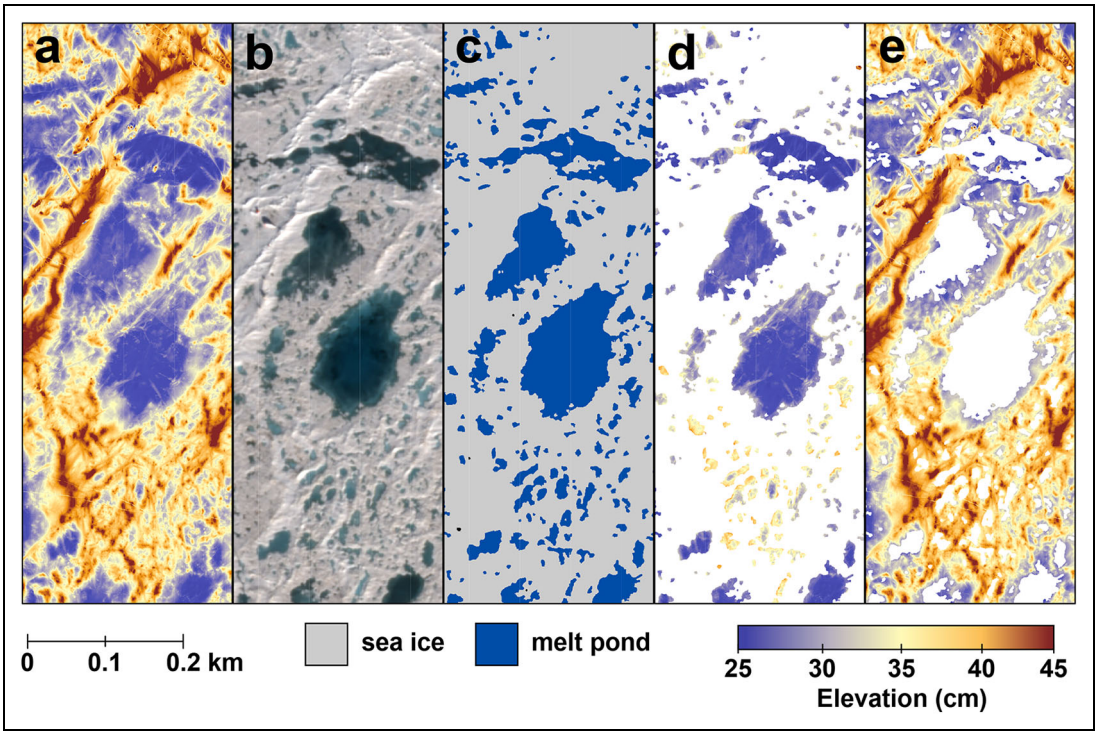

Figure 4. Relating spring surface roughness conditions to summer melt ponding. (a) Surface elevations from the airborne laser scanner on April 8, 2020. (b) Planet Lab, Inc. satellite image from July 1, 2020, during near-maximum pond coverage. (c) Surface classification results of ponded ice and bare sea ice following Wright et al. (2020). (d) The resulting masked surface elevations for the (d) ponded and (e) bare ice surfaces. DOI: https://doi.org/10.1525/elementa.2021.000072.f4

survey line was mostly first-year sea ice (FY) and a mixture of deformed and level ice (Nicolaus et al., 2022). For a comparison of FY and SY ice, measurements collected from "A" to "B" in **Figure 2** were identified as SY ice, while measurements along the Lemon Drop albedo line at "C" to the end of the survey route at "D" were considered primarily

FY ice. These delineations of ice types are based on the initial state of the floe when CO1 was first established in October 2019, by the presence of sediment, and the wintertime salinity profiles (Nicolaus et al., 2022; M Oggier, personal communication, December 1, 2021). Approximately 1 km of distance was measured for each ice type, equating to approximately 750 point measurements.

From June 29 onward, transect data were nominally collected four times per week. The number of point measurements was approximately 1,500 on average and ranged from 782 to 2,656. The last date of a complete survey was July 26, yielding 18 complete surveys capturing the evolution of a snow-covered surface to a mostly snow-free, ponded icescape. Poor visibility and polar bear activity prevented complete surveys on July 16, 23, 24 and 27. The floe edge progressively eroded away over time due to melt and dynamics, forcing detours on July 25 and 26. On July 13–14 and July 19, subnivean ponds were not documented (Section 2.4).

To supplement transect data, ruler (Smith et al., 2021) and magnaprobe measurements parallel to the 200-m albedo lines were incorporated into the analysis. When data from both albedo lines were present and observations of subnivean ponds were consistent with the definition in Section 2.4, the data were incorporated into the time series. As an example of the data differences, Figure S1 shows the snow/SSL depth comparison between the transect route, Lemon Drop albedo line, and Root Beer Barrel albedo line. The albedo line measurements were collected manually and with a magnaprobe. Compared to the transect data, the Lemon Drop line had thin snow/SSL depths and deep melt pond depths, while the Root Beer Barrel line showed deep snow/SSL depths and shallow pond depths. Their collective mean is within the seasonal mean and standard deviation of the transect measurements; the snow/SSL fraction and depth from the albedo lines were 73 $\pm$ 9% and 7 $\pm$ 3 cm, respectively, while the transect results yielded 81 $\pm$ 8% and 8 $\pm$ 4 cm.

2.2.2. CO3: Summer-to-autumn freeze

CO3 was established at 104.5°E, 88.0°N (**Figure 3**) and was composed primarily of level FY ice (Nicolaus et al., 2022). A new transect route was established for monitoring the changes in snow depth, sea-ice thickness, and melt pond depth during the onset of freezing. Ice dynamics created cracks, leads, and shearing from the onset of the camp installation. The initial transect route separated and drifted away, and a new grid was established on August 24. To balance the needs for a transect time series, large-scale sampling, and the limited working area of CO3, a comparatively smaller grid area (approximately 100 m by 200 m) was measured weekly, averaging 335 point measurements, while approximately 1.5-km-long surveys were conducted outside of CO3 for larger-scale characterization of surface conditions, yielding an average of 1,173 point measurements. These latter surveys were each unique, with different routes. Data from the small grid and off-floe surveys were incorporated into the analysis. Surveys began when melt ponds were still present on August 24 and ended on September 19, shortly after the onset of continuous freeze. Multi-kilometer surveys were conducted at three ice stations on September 24, 26, and 30 while transiting out of the ice pack (**Figure 3**).

2.3. Other sources of melt pond observations

The data sets used in larger-scale melt pond comparisons include retrievals of melt pond fractions from National Technical Means (NTM; USGS Global Fiducials Library) and commercial (DigitalGlobe NextView; Planet Labs, Inc.) satellite imagery, and pond fractions and depths from the Surface Heat Budget of the Arctic Ocean (SHEBA) expedition, which was a year-long drift experiment on multiyear (MY) sea ice in the Beaufort and Chukchi seas in 1997–1998 (Uttal et al., 2002). The NTM imagery was collected at the 2011 joint NASA Operation IceBridge and U.S. Naval Research Laboratory "Determining the Impact of Sea Ice Thickness on the Arctic's Naturally Changing Environment" field campaign, located near the APLIS/Naval Ice Experiment (ICEX) ice camp (Gardner et al., 2012). The NTM imagery was processed for melt pond fractions following Webster et al. (2015), while the Planet imagery was processed following Wright and Polashenski (2018) using the Open Source Sea-ice Processing (OSSP) algorithm. Both approaches yield an average accuracy of 98% and, in previous unpublished work (not shown), the results between algorithms showed strong agreement.

The Planet SkySat scenes are composites of 60 overlapping frames covering an area of approximately 7 km by 15 km with 1-m resolution or better. SkySat imagery is 4-band multispectral, observing the blue, green, red, and near-infrared wavelengths. The NTM image scenes are panchromatic and cover approximately 15 km by 15 km with a 1-m resolution. Most satellite scenes analyzed in this work were composited, yielding a total coverage of 100–200 km^2. The SHEBA pond observations come in two forms: (1) areal fractions derived from airborne and satellite imagery in mosaics roughly 10 km by 10 km with submeter resolution (Perovich et al., 2002b), and (2) areal fractions and depths averaged over a 200-m albedo survey line (Perovich et al., 2003).

2.4. Model output

The seasonal evolution in pond coverage was compared between observations and model output from Version 2 of the Community Earth System Model (CESM2) (Danabasoglu et al., 2020) and the Marginal Ice Zone Modeling and Assimilation System (MIZMAS) (Zhang et al., 2018). Two CESM2 grid cells were chosen for the comparison, each representing CO2 and CO3 locations. Due to the comparatively higher spatial resolution of MIZMAS, grid cells that overlapped with the drift tracks in space and time were selected for the comparison.

CESM2 experiments were run using the CAM6 atmospheric component at 1° horizontal resolution. The ocean and sea-ice model components also have a nominal 1° resolution. The standard CESM2 model is described in Danabasoglu et al. (2020), and the CESM2 large ensemble is described in Rodgers et al. (2021) and at the following

website: www.cesm.ucar.edu/projects/community-projects/LENS2/. The sea-ice component of CESM2 uses the Los Alamo Sea Ice Model (CICE5; Hunke et al., 2015), which is a dynamic-thermodynamic model that uses elastic-viscous-plastic dynamics (Hunke and Dukowicz, 2002) and a sub-grid scale ice thickness distribution. CICE5 uses mushy layer physics to simulate sea ice and incorporates prognostic salinity (Turner et al., 2013; Hunke et al., 2015; Bailey et al., 2020). Melt ponds are parameterized assuming a depth-area ratio for pond volume and are carried as tracers on the level portion of each sea-ice thickness category (Hunke et al., 2013). Rain and meltwater from snow and sea ice are a source for melt ponds, while drainage through permeable ice and off floe edges into the ocean are sinks. Pooling meltwater can infiltrate the snowpack, simulating the emergence of melt ponds during spring melt. Simulated freeze-up of melt ponds includes ice lid formation on which snow can accumulate and subsequently shield the ice lid, melt pond, and underlying ice from solar radiation. For comparison to field data, we assessed simulated pond conditions using the "effective pond fraction" variable, which is the pond fraction used in the radiative transfer calculation and not included as a standard-requested variable in Sea-Ice Model Intercomparison Project (SIMIP) (Notz et al., 2016). We conducted this analysis for a grid cell in the vicinity of the MOSAiC and SHEBA sites for simulation year 2015. We used 30 ensemble members from the CESM2 large ensemble (Rodgers et al., 2021) to account for the influence of internal climate variability on the simulated melt pond evolution.

MIZMAS is an ice/ocean modeling and assimilation system based on the Pan-arctic Ice/Ocean Modeling and Assimilation System (PIOMAS; Zhang and Rothrock, 2003). The MIZMAS grid uses a generalized orthogonal curvilinear coordinate system with the North Pole of the model grid displaced in Alaska. This grid yields an average of approximately 20-km resolution between the different locations of CO2 and CO3. The ocean component is based on the Parallel Ocean Program (POP; Smith et al., 1992). The sea-ice component is a thickness and enthalpy distribution sea-ice model (Hibler, 1980; Zhang and Rothrock, 2003) with eight sub-grid scale categories of ice thickness, ice enthalpy, and snow distribution for each grid cell. Similar to the treatment of the sub-grid scale property distributions, MIZMAS incorporates an eight-category melt pond distribution conservation equation (Zhang et al., 2018). Unlike the prescribed treatment of melt ponds in PIOMAS, the equation in MIZMAS accounts for changes in melt pond distributions due to ice motion, ice growth, ice and snow melt, ice ridging, rainfall, and pond drainage; more details can be found in Zhang et al. (2018). As MIZMAS is forced by reanalysis (National Centers for Environmental Prediction (NCEP) Climate Forecast System: Saha et al., 2014) and uses data assimilation, it is expected to match the observed sea-ice state more closely than the free-running CESM2, where the sea-ice evolution differs from the real world in a given year.

3. Results and discussion

The results and discussion are organized in the following order: Sections 3.1 and 3.2 present the chronological evolution of snow/SSL and melt ponds, from summer melt to autumn freeze-up; Section 3.3.1 places the MOSAiC observations into context through comparisons with airborne and satellite observations; and Section 3.3.2 reveals the differences between the MOSAiC observations and output from widely used sea-ice and global climate models.

3.1. Spring-to-summer melt season (CO2)

Prior to melt in early May, the average and standard deviation snow depth was 32 $\pm$ 18 cm (n = 899) on the CO1 Northern Loop. The small overlap between the CO1 Northern Loop and CO2 transect is shown in **Figure 2**, with a snapshot of snow and sea-ice thickness conditions from May 7 and July 20 shown in **Figure 5**. Shortly after May 25, a multi-day period of above-freezing temperatures and rainfall occurred, which reduced the snowpack and preconditioned the surface for melt pond formation. Widespread ponded surfaces were visible in satellite imagery on May 28 (Figure S2). Although snowfall and freezing conditions followed shortly after, masking the surface with fresh snow, melt ponds later formed in these same locations once continuous melt ensued. The remainder of the melt season was characterized by above-freezing temperatures, fog, rain, and mostly cloudy conditions (Rinke et al., 2021; Shupe et al., 2022).

The first surveys on June 17 showed that the average snow depth had reduced to 18 $\pm$ 17 cm from pre-melt values. Thereafter, the melting snow cover steadily decreased in depth and areal coverage as it ablated and revealed the developing SSL underneath (**Figures 6a** and **7**). A scant snowfall event occurred on June 27, but it had a negligible effect on the snow-depth time series. The snow/SSL decreased to a minimum depth of 4 $\pm$ 2 cm by July 26. Throughout the melt season, the snow/SSL remained thicker and more variable on SY ice than FY ice (**Figure 8**).

Snow depth distributions became less heterogeneous over time as shown by the 2-cm standard deviation in thickness in late July. Even so, a few snow drifts by ridges persisted throughout the melt season. To estimate the fractional coverage of drifts and snow they contained, we considered drifts to be at least one standard deviation deeper than the mean snow depth on a given day (**Figure 6a**). On average, drifts covered about 16% of the transect route and contained 33% of the surveyed snow by mid-July, owing to the loss of snow on level ice surfaces and persistence of drifts in deformed ice areas. Although some snow drifts persisted during summer, their structural composition was not typical of a highly reflective snow cover (Perovich et al., 2002a); these drifts were composed of extremely coarse grains 1–2 cm in diameter. With or without snow drifts, the mean thickness of the snow/SSL by late July was 5 $\pm$ 3 cm, which is consistent with previous observations of a 1–10-cm thick SSL during the SHEBA expedition (Light et al., 2008). By July 26, the areal fraction of snow/SSL had reduced to a minimum of 78% (**Figure 7**).

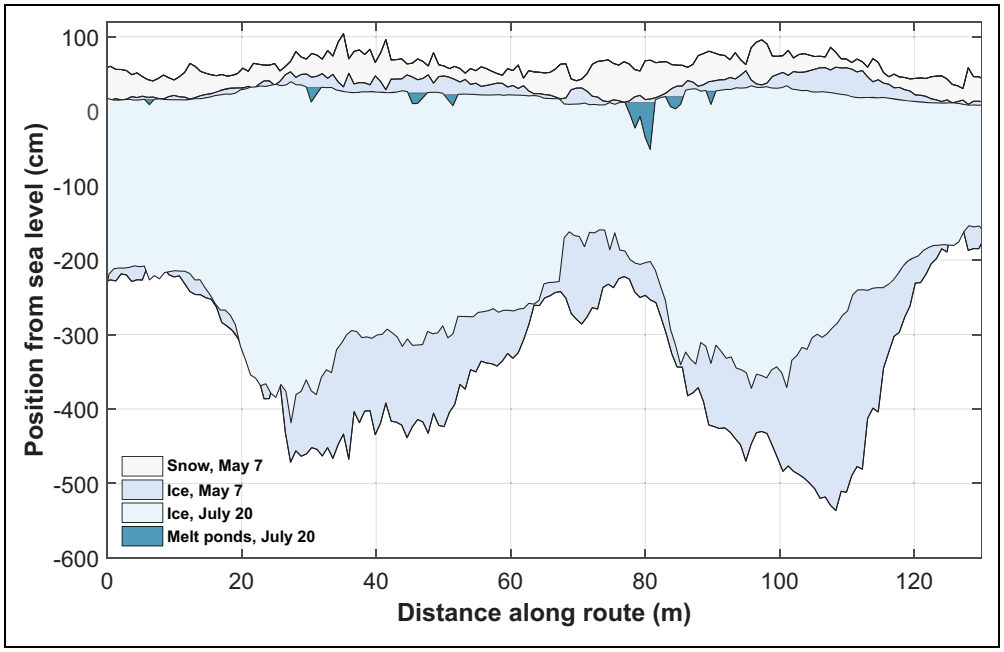

Figure 5. Snow depth, sea-ice thickness, and melt pond depth before and after melt. Snow depth, sea-ice thickness, and melt ponds from an overlapping section between the Northern Loop of Central Observatory 1 and the transect of CO2 on May 7, before melt onset, and on July 20, during an advanced state of melt. By July 20, most snow had melted away entirely to reveal a bare ice surface with a well-developed surface scattering layer. DOI: https://doi.org/10.1525/elementa.2021.000072.f5

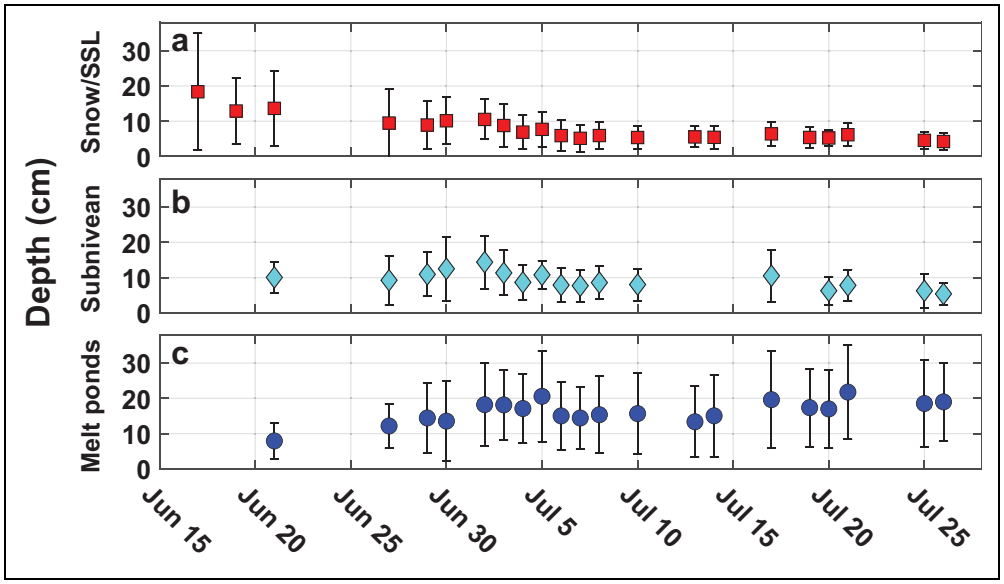

Figure 6. The June–July changes in snow/SSL, subnivean pond, and melt pond depths along the transect route. Time series of the mean and standard deviation (error bars) of the (a) snow and surface scattering layer (SSL) depths (red squares), (b) subnivean pond depths (aqua diamonds), and (c) melt pond depths (blue circles) during the melt season on Central Observatory 2. DOI: https://doi.org/10.1525/elementa.2021.000072.f6

Subnivean ponds underwent a more variable transition in depth and coverage relative to the snow/SSL. This transition was intimately linked to the formation and evolution of melt ponds and, to a lesser degree, meteorological conditions. Although observed earlier, subnivean ponds were first recorded on June 19 and preceded the widespread formation of melt ponds (**Figure 7**). The areal fraction peaked at 15% coverage and remained higher than that of melt ponds for the earlier part of the melt season. The depth of subnivean ponds was also larger than that of melt ponds during the early melt season. However, as melt ponds formed and deepened and the snowpack melted away, the depth of subnivean ponds steadily declined (**Figure 6b** and **c**).

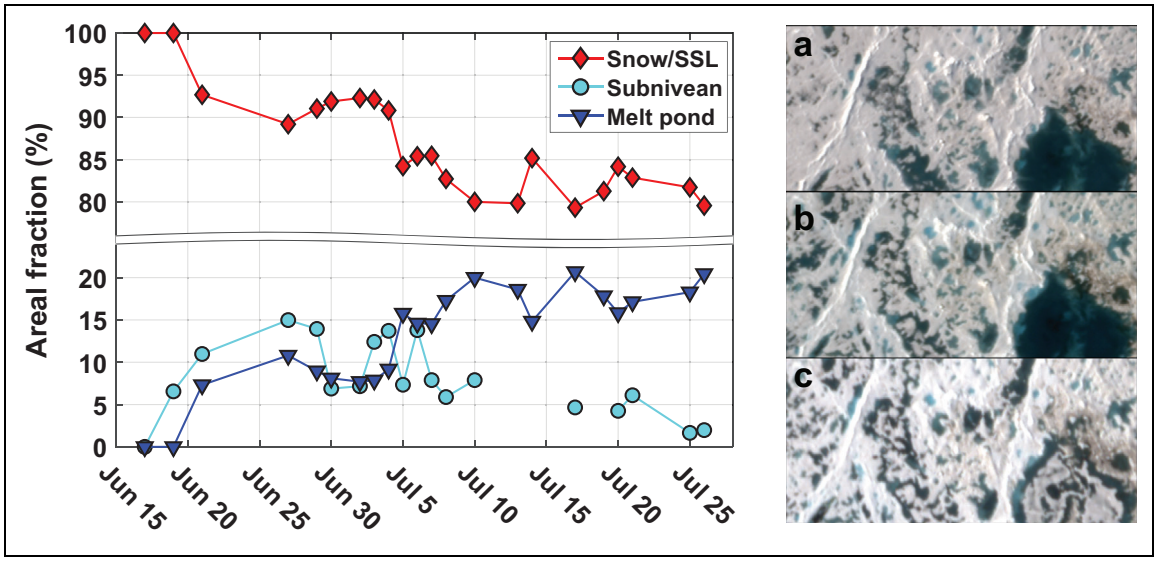

Figure 7. Time series of areal fractions of different surface types during the melt season. Left: Areal fractions of the three surface types of snow/surface scattering layer (SSL; red diamonds), subnivean ponds only (aqua circles), and melt ponds (blue triangles), during the June–July melt season, as determined on Central Observatory 2. The snow/SSL category includes the area covered by subnivean ponds. Right: A subset of multispectral Planet Lab imagery of the transect route for (a) July 1, (b), July 7, and (c) July 22. The width of the image scenes is approximately 340 m. In between these dates, some ponds drained while others formed and grew. DOI: https://doi.org/10.1525/elementa.2021.000072.f7

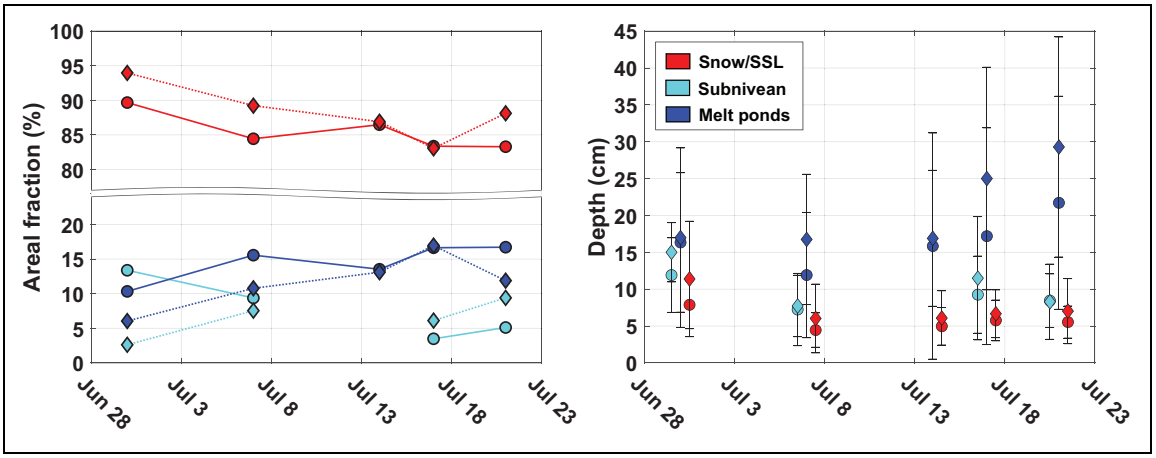

Figure 8. Time series of areal fractions of different surface types between ice types. Left: Areal fractions of different surface types for second-year (diamonds) and first-year (circles) sea ice, as depicted in **Figure 4**. Right: The mean thicknesses or depths of snow/surface scattering layer (SSL), subnivean ponds, and melt ponds for second-year (diamonds) and first-year (circles) sea ice. The standard deviation is shown by the error bars. DOI: https://doi.org/10.1525/elementa.2021.000072.f8

Interestingly, the areal fraction of subnivean ponds was substantially greater on FY ice than SY ice (13% versus 3%) during the early melt season (**Figure 8**). We attribute this difference to the ability of meltwater to spread more extensively on smoother surfaces relative to the rough surface relief typical of SY and MY ice. Indeed, ALS surface elevations from April 8, 2020, showed that the SY ice was approximately 43% rougher than FY ice along the transect route. Rough surface topography can constrain the lateral transport of surface meltwater and area in which meltwater can pool (Eicken et al., 2004; Polashenski et al., 2012; Webster et al., 2015). By late July, the areal fraction of subnivean ponds was higher on SY than FY ice, which is likely related to the deeper, more variable snow/SSL that persisted longer on SY ice (7 ± 4 cm) than the more uniform snow/SSL observed on FY ice (6 ± 2 cm) (**Figure 8**).

On June 30, clear skies and lower air temperatures led to the refreezing of the surface and a notable decrease (7%) in the areal fraction of subnivean ponds and a modest

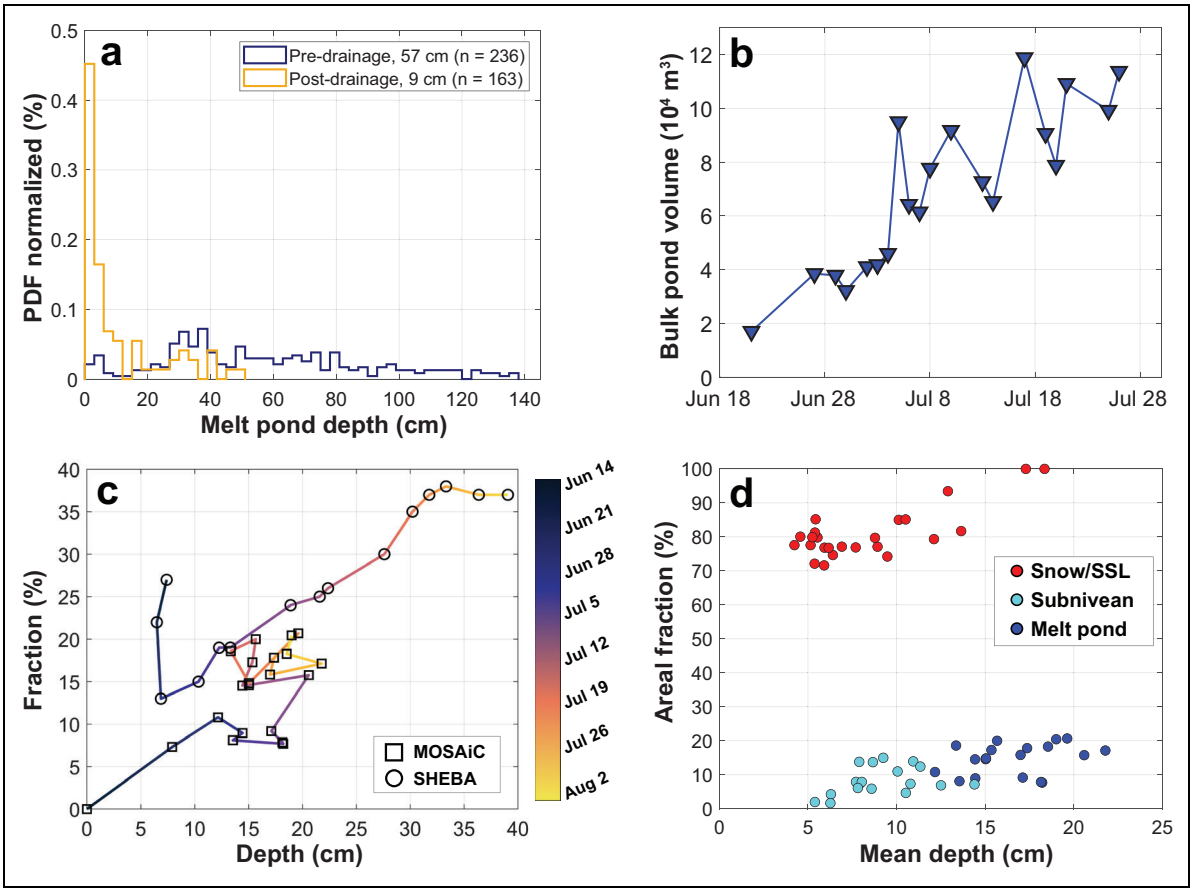

Figure 9. Melt pond characteristics relevant to meltwater storage and model parameterizations. (a) The change in the distribution of pond depths measured on a grid survey of a large pond on Central Observatory 2, before and after the vertical drainage event on July 11–13. Depth measurements were collected on July 9 and 13. Bin width is 3 cm. (b) The bulk (total) volume of pond water based on the average areal pond fraction, pond depth, and area of CO2. (c) Melt pond areal fractions and mean melt pond depths during summer melt from the 200-m survey line at SHEBA and the MOSAiC transect route. (d) The mean areal fractions as a function of mean depth of different surface types on the transect route. DOI: https://doi.org/10.1525/elementa.2021.000072.f9

decrease (about 1%) in melt pond coverage. Small ponds and ponds with lateral drainage channels were noticeably shallower on this date (**Figure 1b** and **c**). In these cases, the distances between the pond water surface and pond ice lid were 1–2 cm, which suggests the continuation of lateral drainage and/or vertical percolation of meltwater despite freezing surface conditions. Over the next few days, heavy rainfall (approximately 24 mm) ensued and a coincident increase in areal fraction and depths was observed in both subnivean ponds and melt ponds. The mean thickness of subnivean ponds reached 14 ± 9 cm during this time, but decreased, albeit variably, for the remainder of the season to a minimum of 5 ± 3 cm on July 25 (**Figure 6b**).

The stages of melt pond evolution described in Eicken et al. (2002) and Polashenski et al. (2012) occurred at different times in different melt ponds across the floe (**Figure 7a–c**). Similar to the findings in Webster et al. (2015), some melt ponds were in the beginning stages of formation while others were undergoing lateral and vertical drainage, with the differences being attributable to variations in sea-ice topography and permeability. Despite variable melt pond behavior, a notable vertical drainage event occurred during windy, rainy conditions (12 m s^{-1} wind speeds, approximately 5 mm water equivalent) on July 11–13. During this event, large melt ponds exceeding 50–100 m in diameter experienced vertical drainage (**Figure 9a**), either through flaw holes or interconnected brine channels. The amount of pond water drained from one of these large ponds was approximately 14,200 m^3; its area decreased from approximately 25,700 m^2 to 5,300 m^2. Although none of these large ponds were measured directly on the transect route, some were connected to surveyed ponds via lateral drainage channels. Thus, there were indirect hydrological effects on the surveyed melt ponds during the drainage event. Based on the mean pond depth and areal fraction from the transect data (**Figures 5** and **6)**, the drainage roughly equated to a bulk meltwater volume loss of approximately 26,500 m^3 (**Figure 9b**).

After the drainage event, areal pond fractions decreased from 21% to 15%, which consequently increased the area covered by a more reflective bare ice/SSL surface (**Figure 7**). Similar to the findings in Perovich et al. (2003), while areal pond fractions instantly decreased during the main drainage event, the mean depth of surveyed ponds changed

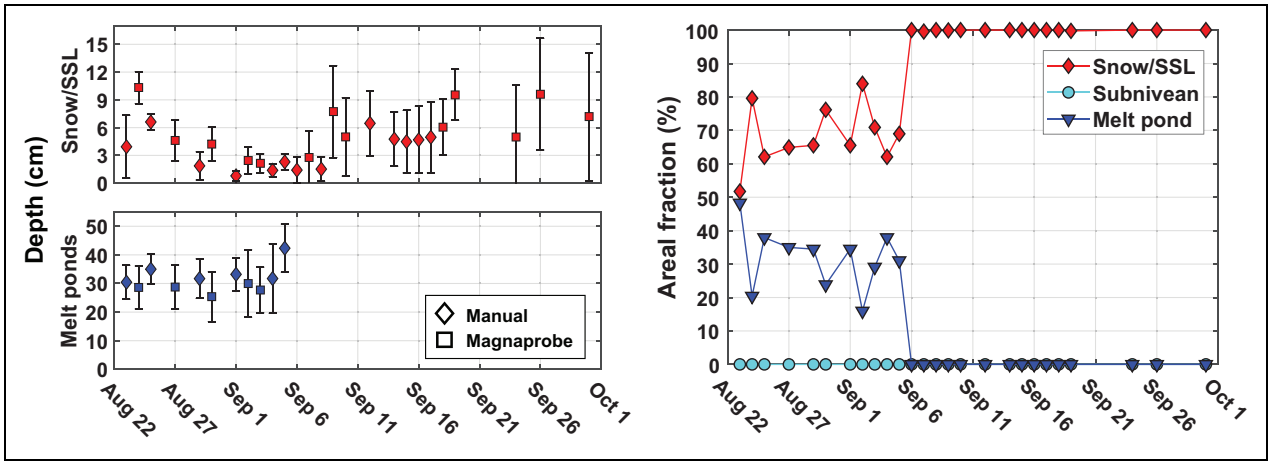

Figure 10. Time series of depths and areal fractions of different surface types during the freeze-up season. Left: Time series of mean snow and surface scattering layer (SSL) depths (red symbols) and melt pond depths (blue symbols) for the August–September freeze-up season, as measured on Central Observatory 3. The standard deviation is shown by the error bars. The different symbol shapes represent different measurement types: manual (diamond) and magnaprobe (square). Right: Areal fractions of surface types during the August–September freeze-up season. Subnivean ponds were not encountered on CO3. DOI: https://doi.org/10.1525/elementa.2021.000072.f10

very little (by approximately 1 cm; **Figure 9c**). Over the course of the melt season, pond depths generally increased over time, and many melted through the ice by late July (**Figures 1d** and **6c**).

On July 26, melt ponds reached a maximum 21% coverage and a depth of 19 ± 11 cm, despite a thin 3–5 mm layer of ice on the ponds. On July 31, CO2 disintegrated due to melt and ocean swell. As a comparison, the maximum melt pond coverage during SHEBA was 24% on August 7 (Perovich et al., 2002b). On CO2, the maximum pond depth was 22 ± 13 cm on July 21, with a breakdown of pond depths being 29 ± 14 cm and 22 ± 14 cm for SY and FY ice, respectively (**Figures 5** and **7**). We note that on July 25–26, the transect route was partially altered due to some FY ponds having melted entirely through (**Figure 1d**).

For most of the melt season, a few unusual surface types along the transect route remained free of snow, an SSL, and pond water. These ice surfaces appeared to be either drained melt ponds, remnant ice broken from the bottom of melt ponds from the previous year which had become frozen into the following year's ice surface, or, especially in refrozen cracks, candle ice, a kind of rotten, columnar-grained ice that forms due to impurities facilitating melt at grain boundaries (USACE, 2002; Figure S3). The zero-thickness surfaces made up less than 1% of the survey route during the melt season and are consistent with similarly unique features observed during the SHEBA campaign.

Continuation of measurements was not possible after the disintegration of CO2, and the *Polarstern* relocated northward for the freeze-up season to establish CO3. CO3 was located at considerably higher latitudes than CO2 (**Figure 3**) and, unlike CO2, was comprised mostly of undeformed FY ice. Consequently, the differences in geographic location and sea-ice conditions should be considered when examining the time series presented in this study. The implications of these differences include earlier freeze-up and snow accumulation at CO3 than CO2, less total insolation at CO3 than CO2, and different melt pond coverage due to differing ice types and surface roughness conditions.

3.2. Summer-to-autumn freeze-up season (CO3)

The time series of surface conditions during freeze-up was more complex than during the melt season due to a combination of variable weather conditions and measurement constraints on CO3. The survey area proved to be too small to yield a representative areal fraction. Given these circumstances and the widespread presence of level FY ice on CO3 and neighboring floes, the transect data were combined with data collected along the Kinder albedo line (Nicolaus et al., 2022) and from larger surveys on nearby floes (**Figure 10**). While the supplementation improves the robustness of the time series, some variation from the limited sample area persists, most notably on August 24, August 30, and September 2.

The surface on August 21 had a thin, melting snow cover and well-developed, drained melt ponds with 3–5-mm ice lids (**Figure 11a**). The evolution of surface conditions strongly corresponded with the variable weather (Figure S4). Initial surveys yielded pond fractions of 35–48%, considerably higher than those observed on CO2. We attribute the higher pond coverage to sea ice being less deformed on CO3. Melt pond coverage decreased to approximately 31% before thick ice lids formed (**Figure 10**). Smaller, shallower ponds formed ice lids first, followed by pond lids forming on larger, deeper ponds. In addition to an apparent dependency on pond size and depth, the location and rate of ice lid formation within a given pond was strongly influenced by wind speed and direction during freezing conditions (**Figure 11b**).

Lower temperatures and snowfall occurred on August 23–24, increasing the snow/SSL to 6 ± 1 cm, and

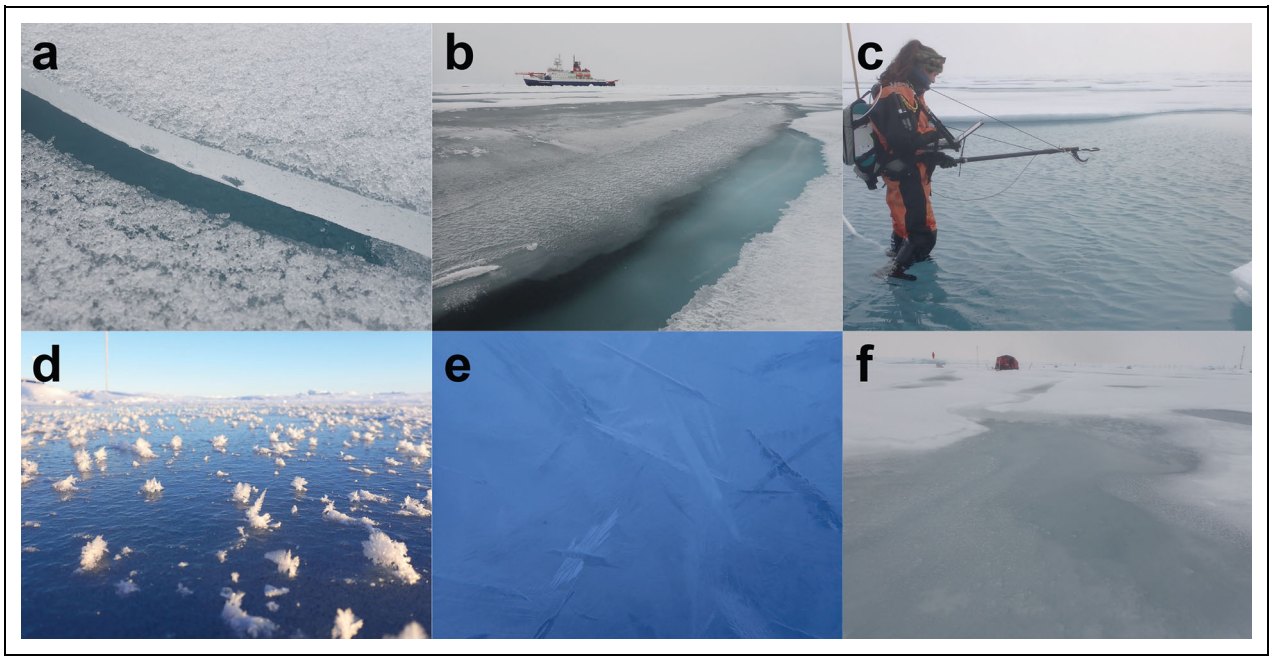

Figure 11. Ephemeral weather events that altered the surface conditions during the autumn season. (a) A melting snow cover and thin pond lids present at the beginning of Central Observatory 3 in mid-August. The pond lid shown was about 2 cm in thickness. (b) Wind speed and direction affected the formation of ice lids over melt ponds, (c) most pond lids had melted away by late August, (d) freezing temperatures and calm conditions in early September allowed frost flowers to form on pond lids and frozen leads, and (e) platelet ice crystals were present in ponds with thaw holes and cracks. The platelet crystals were about 1–3 cm in length. (f) In mid-September during above-freezing temperatures and heavy rainfall, the snow cover on refrozen melt ponds became saturated, turned into slush, and, in many cases, melted away. The tent (approximately 3.5 m × 3.5 m × 2.0 m) in the background provides scale. DOI: https://doi.org/10.1525/elementa.2021.000072.f11

decreasing pond fractions by 10% (**Figure 10**). However, this snowpack formation was short-lived. Above-freezing temperatures and intermittent rainfall lead to a steady reduction in the snow/SSL and a "re-opening" of melt ponds as their ice lids melted away (**Figure 11c**). On September 2–4, the daily maximum air temperatures dropped to between −1.1°C and −0.4°C (Figure S4). As a result, melt ponds formed ice lids again, and the snow/SSL depth became zero due to the magnaprobe being unable to penetrate a frozen SSL. Between September 2 and 8, the snowpack increased incrementally to a 2-cm thickness and frost flowers formed on melt pond lids and refrozen leads (**Figure 11d**). During this time, platelet ice formed in several ponds next to leads and in those containing cracks and thaw holes (**Figure 11e**).

By September 6, all melt ponds had frozen over with at least 5-cm ice lids, and the snow areal fraction reached 100% (**Figure 10**). Even so, liquid water was still present underneath the lids of large ponds for the duration of the CO3 field component. These ponds were also locations where drifting snow created a more variable snow depth distribution, leading to locally deeper snow or snow-free (wind-scoured) conditions relative to surrounding, unponded snow-covered ice. This disproportionate redistribution of snow on ponded versus unponded ice was also observed on the SHEBA expedition (see figure 11d in Perovich et al., 2003) and a field campaign in 2018 (Anhaus et al., 2021).

In mid-September, a cyclone caused a rain-on-snow event (Figure S4). The cyclone had wind speeds of approximately 17 m s^{-1}, high (0°C) maximum air temperatures, and approximately 15 mm (liquid equivalent) of snowfall and rainfall, all of which thinned the snowpack from 8 ± 5 cm to 4 ± 3 cm (**Figure 10**). The largest change in snow occurred over refrozen melt ponds where much of the snow melted into slush (**Figure 11f**). For the remainder of CO3, a mixture of snowfall and freezing drizzle increased the snowpack to a mean depth of 10 ± 3 cm, but the snow cover was still optically thin on September 19 (**Figure 10**; Brandt et al., 2005; Perovich, 2007). In late September, ice station work on the voyage out of the ice revealed comparable, although more variable, snow depth distributions at more southerly latitudes (**Figure 10**).

3.3. Broader comparisons and context

Ground observations are invaluable for documenting local-scale processes and variability, which, in turn, can inform the development and enhancement of model parameterizations and satellite algorithms. However, scaling up to model grid cells and satellite footprints poses a challenge in reconciling sub-grid cell properties to broader aggregate spatial scales (Webster et al., 2022). In this section, we compare melt pond coverage from ground observations with those derived from high-resolution satellite imagery. These results are then used to guide the interpretation of comparisons between ground observations

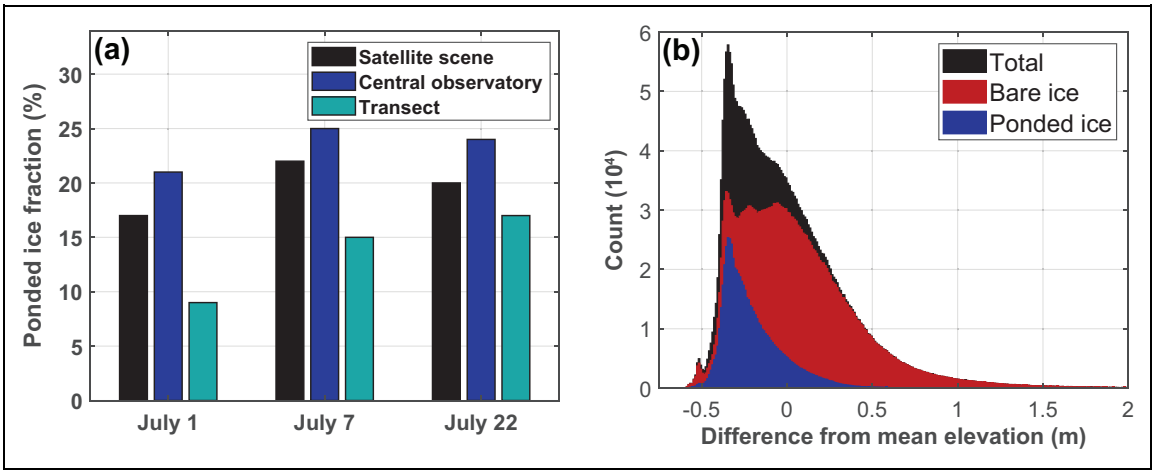

Figure 12. Connections between melt pond fractions and surface roughness. (a) A comparison of ponded ice fractions between the transect data and the Open Source Sea-ice Processing satellite retrievals of the broader MOSAiC area (Satellite scene) and Central Observatory 2. (b) The difference between surface elevations and mean surface elevation of CO2 measured by the airborne laser scanner on April 8, 2020, as a function of surface types retrieved from the satellite image from July 1, 2020. DOI: https://doi.org/10.1525/elementa.2021.000072.f12

and model simulations of melt pond coverage, as well as the sea-ice conditions related to melt pond distributions.

3.3.1. Representation across spatial scales

Melt pond distributions are heterogeneous in space and time. Here, we compare the coverage of melt ponds measured on the transect route with those retrieved from satellite imagery to assess differences across spatial scales. Note that the satellite retrievals of "sea ice" are equivalent to the combination of the observed snow/SSL and subnivean ponds because they have similarly high reflectivity from the nadir view. Despite CO2 being 10% rougher than the broader region in spring, its pond coverage was higher than that in the broader region for all of July. This finding suggests that, although surface roughness is strongly linked to the distribution of melt ponds on a local scale, at larger spatial scales, the relationship between surface roughness and pond coverage weakens. Both CO2 and the broader region (100–150 km^2 in size) exhibited higher average melt pond coverage than what was measured on the transect route (14%), yielding 23% and 20%, respectively (**Figure 12a**).

Across spatial scales, the values observed during MOSAiC are considerably lower than the 2000–2011 mean (30–33%) for July, as derived from the Moderate Resolution Imaging Spectroradiometer (Rösel et al., 2012). The largest difference in pond coverage between spatial scales occurred on July 1, when melt ponds exceeding approximately 100 m in diameter were present on the inner portion of CO2. On June 29, lateral drainage channels were observed along the transect route, which may point to a possible cause for the difference between the ground observations and satellite retrievals: melt ponds near the edge of the floe may drain more readily than those that are isolated and constrained by higher surface relief away from the floe edge. This explanation agrees well with Wright et al. (2020) in that pond-free areas have been commonly observed near ice floe edges.

As melt progressed on CO2, the difference between the ground observations and satellite retrievals became smaller. This increasing similarity across spatial scales suggests that spatial heterogeneity is particularly large during the earlier stages of melt pond evolution when ponds are separate and vary greatly in size. After vertical drainage, spatial heterogeneity in pond size decreases as ponds become highly interconnected, as determined by the smaller standard deviation in pond size distribution in late July. Perovich et al. (2002b) found similar temporal differences in the pond distributions at SHEBA, with the greatest spread in pond area occurring earlier in the melt season.

The largest and deepest ponds on CO2 occurred in areas with low, level surface relief surrounded by ridges. Using airborne surface elevations from April 2020 with optical satellite imagery from July 2020, we found that the mean surface elevation for ponded ice areas was 20 cm lower than that of CO2 (**Figure 12b**). In comparison, pond-free ice areas exhibited a mean surface elevation 5 cm higher than that of CO2. Using the standard deviation as a proxy for surface roughness, the pond-free areas were nearly twice as rough as ponded sea-ice areas, which underscores the relationship between local surface roughness and pond coverage (**Figure 1e**). In addition to surface roughness, several factors influence the distribution, coverage, and depth of melt ponds, including sea-ice permeability, macroscopic flaws (i.e., cracks), and ice thickness. For example, macroscopic flaws in thin, level sea ice can lead to earlier pond drainage and thus smaller pond coverage, as was observed in a small area of FY ice on CO2.

3.3.2. Model-observation assessment

Figure 13 shows the seasonal evolution of the ponded ice fraction from a selection of field campaigns and the CESM2 and MIZMAS simulations. The field campaigns represent different ice conditions, geographic areas, and years. In chronological order, the SHEBA campaign was

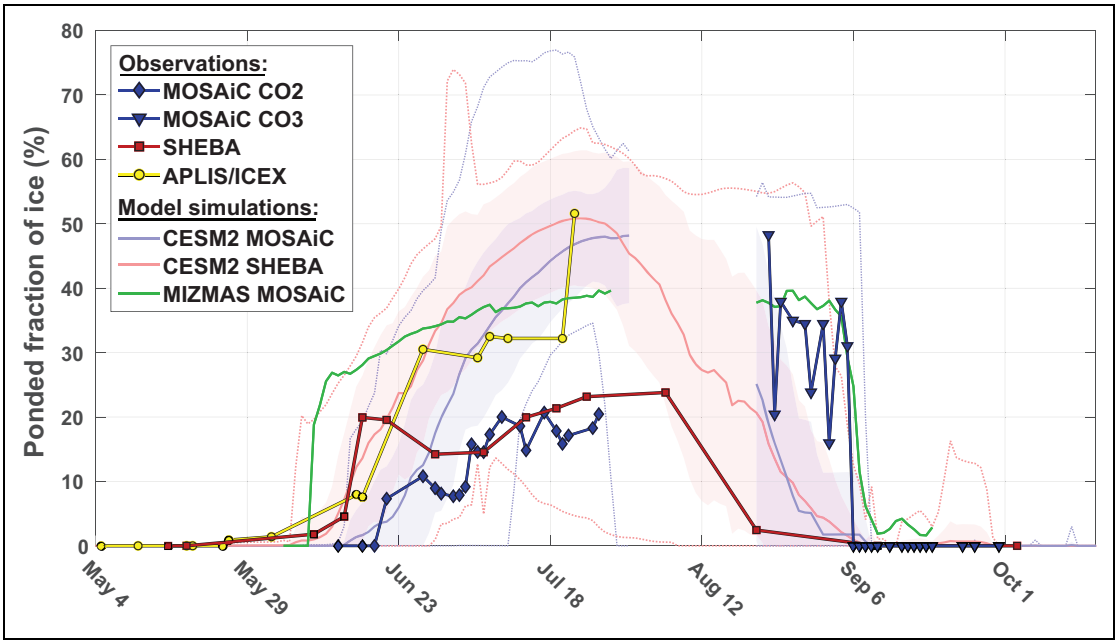

Figure 13. Annual cycle of melt pond fractions from model simulations and observations. A comparison of melt pond fraction values during the melt season between SHEBA (1998, predominantly multiyear ice), ICEX (2011, predominantly level first-year ice), MOSAiC (2020), and model output from CESM2 and MIZMAS. The April–July MOSAiC data and CESM2 MOSAiC results correspond to CO2 (predominantly second-year ice), while mid-August to November results correspond to CO3 (predominantly level first-year ice). The CESM2 SHEBA output corresponds to the SHEBA location. The shading represents the standard deviation across the 30 ensemble members, while the solid and dotted lines represent the mean and range, respectively. DOI: https://doi.org/10.1525/elementa.2021.000072.f13

predominantly MY ice, APLIS/ICEX was mostly level FY ice, MOSAiC CO2 was predominantly SY ice, and MOSAiC CO3 was mostly level FY ice. The comparison of modeled and observed conditions is complicated by the different spatial scales involved, with the models representing conditions over a large grid cell, and, for the coupled CESM2 climate model, by the influence of internal climate variability, which causes challenges when comparing to a single year of observations. Nevertheless, the initial comparison provided here gives insight on potential model biases and emphasizes the need for a more comprehensive comparison to investigate the processes driving simulated pond formation and evolution.

Although ephemeral ponds were visible in satellite imagery on May 28 (Figure S2), continuous pond formation was not observed by satellite or in situ until mid-June. Continuous pond formation also occurs in mid-June in CESM2, but with a 5-day standard deviation and 19-day range. In comparison, continuous pond formation occurs about 1 week earlier in MIZMAS. Both CESM2 and MIZMAS maximum pond fractions exceed the MOSAiC-CO2 observations, reaching 51% and 40%, respectively, on the date of the maximum transect value of 21% in July. The standard deviation in pond coverage across the 30 ensemble members of CESM2 was 8% in late July, while the range was 22–67%. Over the CO2 pond season, the average pond fractions from CESM2 and MIZMAS were 31% and 36%, respectively, compared to observed 14% from surface-based observations. Even when considering that the broader area had higher pond coverage than the transect route (**Figure 12a**), both models still overestimate pond coverage for June–July.

CESM2 simulates a wide range in pond coverage and dates of pond freeze-up in autumn 2015. Here, we define pond freeze-up as the first date at which pond fractions reach zero and remain at zero for the remainder of the year. From August 24 to September 6, the simulated mean pond coverage was 26 ± 22% across the 30 ensemble members. On average, the date of simulated pond freeze-up occurred about 2 weeks earlier than the observations. The larger standard deviation (8 days) and range (33 days) in pond freeze-up, relative to pond onset, likely results from greater sensitivity to internal climate variability, as was similarly found for sea-ice freeze onset and sea-ice melt onset in Version 1 of the CESM large ensemble in Smith and Jahn (2019). The MOSAiC observations show fluctuations of 20% in pond coverage (note, the near-maximum value of pond coverage on CO2) during the freeze-up period due to the high sensitivity of ponds to ephemeral above- and below-freezing conditions during episodic weather (Section 3.2). In comparison, MIZMAS simulates similar pond coverage (37 ± 2%) and pond freeze-up (September 6) compared to observations (32 ± 9%; September 6).

The model and observational results reveal two noteworthy phenomena of seasonal melt pond evolution. First, if average temperatures are above freezing for a sufficient amount of time, pond onset is a steady process with thermal inertia, making pond onset less sensitive to short-lived weather events and thus less variable than pond freeze-up.

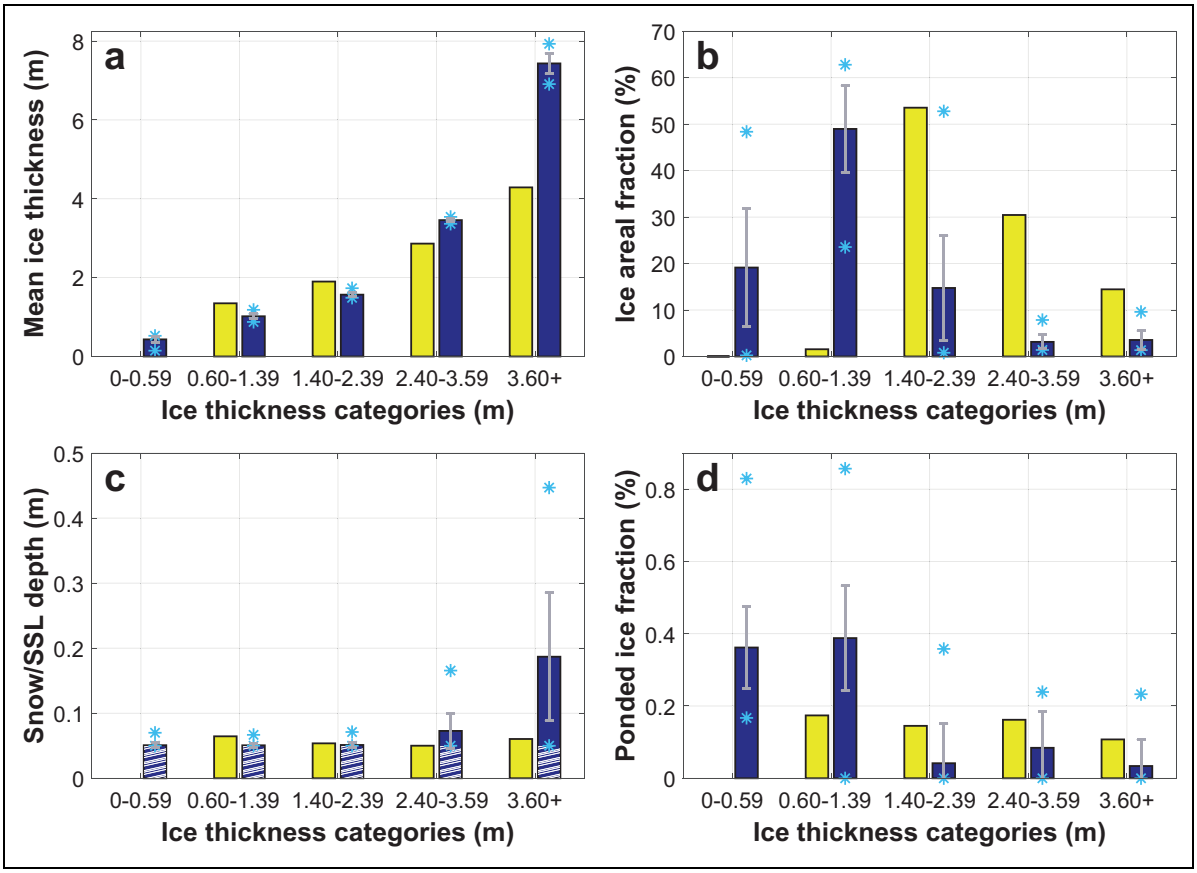

Figure 14. Simulated and observed snow, pond, and ice properties for five ice thickness categories in CESM2 (July 7). Dark blue bars represent the CESM2 model ensemble mean, while the grey error bars represent the standard deviation and the cyan asterisks the range of values across the 30 ensemble members. The yellow bars represent the observed mean value. (a) Mean sea-ice thickness for the five ice thickness categories in CESM2 for the MOSAiC transect data from Central Observatory 2 and CESM2 for July 7, 2020. (b) Areal ice fraction of each ice category. (c) Mean snow/surface scatter layer (SSL) depth per ice thickness category. The observational mean includes the subnivean pond and SSL depths, and the white hatching in the CESM2 results represents a 0.05 m-thick SSL in addition to its (non-hatching) snow depth value. (d) Fraction of ponded sea ice per ice thickness category. Note that the y-axis range differs across all panels. DOI: https://doi.org/10.1525/elementa.2021.000072.f14

The pooled meltwater underneath the snowpack during spring melt is insulated by snow and much of it can remain unfrozen, despite episodic freezing, as was observed during MOSAiC. Second, pond freeze-up is an abrupt process that is highly sensitive to the weather due to the relatively short time that is needed to freeze a thin layer of ice on ponds. Below-freezing temperatures can effectively reduce the pond coverage to zero in a matter of hours. Moreover, for melt ponds that are mostly comprised of freshwater, freezing can occur at 0°C rather than −1.8°C for seawater.

Interestingly, CESM2 produces overly high melt pond coverage at the SHEBA location. On one hand, the discrepancy with the SHEBA observations could be partly due to the simulation year of 2015 rather than the year (1998) of the SHEBA expedition. On the other hand, the overly high pond coverage may point to a possible deficiency in the volume of meltwater being produced and/or retained on the ice, the representation of physics controlling melt pond drainage, the distribution of meltwater across sea-ice thickness categories, or a combination of these factors. We note that the simulated maximum pond coverage at both the MOSAiC CO2 (51%) and SHEBA (55%) sites were more comparable to the 51% pond coverage observed at the APLIS/ICEX site, which was primarily composed of heavily ponded, undeformed FY sea ice.

To explore this latter topic further, we evaluated the sea-ice thickness, snow/SSL depth, and the areal fraction of ponded ice and snow-covered ice as functions of the five ice thickness categories in the CESM2 ensemble members for July 7 (**Figure 14**). The model assumes the presence of an SSL on bare ice, with a fixed SSL thickness of 0.05 m for ice thicknesses greater than 0.80 m. Therefore, 0.05 m was added to the simulated mean snow depth for a more appropriate comparison with the magnaprobe measurements, which cannot distinguish between snow and an SSL in melting conditions. In **Figure 14c**, the white hatching in the simulated snow/SSL depths represents a 0.05-m thick SSL.

The model-observation comparison shows notable differences in the ice thickness distribution. The observed sea-ice thickness on the transect route was greater than 0.6 m and, consequently, no observational data apply to the 0–0.59-m thickness category from the model (**Figure 14a** and **b**).

We therefore omit a comparative analysis of snow depth and melt ponds in the 0–0.59-m ice thickness category. The remaining ice thickness categories show considerable differences in their fractional coverage (e.g., observed 2% versus simulated 48 ± 9% areal coverage of sea ice in the 0.6–1.39 m range). In general, CESM2 overestimates the amount of ice thinner than 1.4 m and underestimates the amount of ice thicker than 1.4 m. Consistent with the findings in DuVivier et al. (2020) and DeRepentigny et al. (2020), the CESM2 simulations submitted to the Coupled Model Intercomparison Project (CMIP6) have Arctic sea ice that is biased thin compared to observations. Despite this thin bias, we note that the thickest ice category (≥ 3.6 m) in the CESM2 simulations has a mean and standard deviation of 7.4 ± 0.3 m, which is substantially larger than the observed 4.3-m thickness.

For snow, CESM2 consistently simulates a 0.05-m thick snow/SSL depth for ice thinner than 2.4 m, which is in strong agreement with the observations (**Figure 14c**). For the thicker ice categories, however, CESM2 simulates a deeper, more widespread snow cover. For example, in the thickest ice category (≥ 3.6 m), the mean snow/SSL depth simulated by CESM2 is 0.19 ± 0.10 m and covers 87% of the thickness category. In comparison, the observed snow depth is 0.06 m for ice thicker than 3.6 m. Given that the thickest ice category comprises less than 5% of the grid cell area, its large bias in snow depth has minimal effect on the grid cell average. Model-observation comparisons in Webster et al. (2021) show that the CESM2 simulates an overly thin and overly uniform snow distribution. Consistent with these findings, the CESM2 snow depth time series (not shown) exhibits overly thin snow in late spring, which has implications for surface albedo and spring melt.

The ponded ice fractions per ice thickness category show a more complex story (**Figure 14d**). Relative to the observations, simulated ponds are distributed across ice thickness categories more heterogeneously, exhibiting 3–39% range in the mean areal fraction while the observed range was 11–17%. Although sea ice exists in all thickness categories across all 30 ensemble members, it is only in the thinnest (0–0.59 m) ice thickness category for which all model years consistently produced melt ponds. Considering the 0.60–1.39 m thickness category (**Figure 14d**), the average and standard deviation in pond coverage is 39 ± 14%, with a range of 0–86%. In comparison, the observed pond coverage was 17%, or nearly half the simulated mean coverage in the 0.60–1.39-m thickness category. This difference indicates a high bias in melt pond coverage for thinner ice categories in CESM2, which may result from there being: (1) too much thin ice in CESM2, as discussed in DuVivier et al. (2020); (2) too many melt ponds on the level ice portion, which is predominantly in the thinner ice categories; (3) too much surface melt; and/or (4) too much meltwater retained on the surface. In the thicker ice categories, the observed pond fraction is within the ensemble spread, suggesting that the simulated pond fractions are comparable to observations. Even so, the simulated mean pond fraction is half, at most, of the observed mean pond fraction for sea ice with a thickness of 1.4 m and larger.

The implications of model-observation comparison suggest that overly thin ice and excessive pond coverage in CESM2 may lead to an overly low surface albedo, whereas thicker ice may produce an overly high albedo due to limited pond coverage and an overabundance of snow. These factors may have compensating effects when simulating surface albedo (Light et al., n.d.). Potential sources of these biases include the: representation of melt ponds on the level portion of sea ice, snow and ice surface melt rates in relation to the representation of albedo, amount of meltwater retained on the surface, and parameters controlling lateral and vertical melt pond drainage. Model experiments that simulate a more realistic sea-ice cover can greatly aid investigations involving the identification of deficiencies and enhancement of sea-ice parameterizations. Recent work by Kay et al. (2022) demonstrated improvements in the CESM2 sea-ice climatology and 20th–21st century transient evolution, with little influence outside of the Arctic, through the tuning of parameters that affect snow grain size. Evaluation of these data, together with the CESM2 large ensemble, is a consideration for future work.

4. Conclusions

This paper provides a detailed analysis of the summer and autumn evolution of surface conditions on the MOSAiC Central Observatories. We investigated the changes in the snow/SSL and melt ponds from spring melt (CO2) to autumn freeze-up (CO3) using in situ transect data, relating the changes to environmental conditions including surface roughness, sea-ice thickness, and weather. To summarize the observed pond evolution, we describe the following key stages:

1. Short-lived melt in late May formed subnivean ponds, where meltwater pooled in surface depressions beneath the snow cover, and open ponds, both of which pre-conditioned the surface for later melt pond evolution.
2. Freezing conditions and late spring snowfall allowed pond lids to form and accumulate snow, masking the uppermost surface with a fresh snow layer.
3. Continuous melt from mid-June formed new open ponds, expanded existing melt ponds, and transitioned the snow-covered surface to a melting ice surface with an SSL, which likely began developing underneath the snow during earlier melt.
4. Lateral drainage channels allowed ponds near the floe edge to drain, while isolated ponds lacking drainage channels continued to expand in area, creating a large distribution in melt pond size.
5. A vertical drainage event in mid-July reduced the mean areal pond coverage and depth modestly and temporarily, and decreased the heterogeneity in pond coverage and size distribution across spatial scales.

6. The continuation of melt into summer deepened melt ponds, causing some to melt completely through the underlying ice to form pockets of open water within the floe matrix.
7. Freeze onset in August caused the SSL to refreeze into the upper sea-ice structure and ponds to abruptly form ice lids and accumulate snow, with drifting snow depositing on most of the lower-lying surface relief of pond lids.
8. During continuous freezing in September, snow depths became deeper over pond lids than pond-free sea ice. Liquid water remained present underneath pond lids and snow, revealing that, although refrozen at the surface, melt ponds required considerable time to cool sufficiently to freeze internally.

We assessed the representativeness of in situ melt pond observations from the summer melt season (CO2) through comparisons with satellite retrievals, showing that, compared to the broader area, average summer pond coverage along the transect was lower (20% versus 14%). Does this finding mean that satellite retrievals tend to overestimate pond coverage because of the derivation over a broader area, or that in situ observations tend to underestimate pond coverage because of local characteristics along survey lines? To shed light on these questions, an expansion of efforts to monitor the evolution of melt ponds through satellite and in situ observations and analyses is needed. In particular, using high resolution (< 3 m) optical imagery to track drifting field programs and autonomous systems (e.g., buoy arrays) can help to reveal the common mechanisms (i.e., variable weather) and properties (i.e., snow depth, roughness) that control melt pond evolution. Equally valuable is targeting a wide range of sea-ice conditions across the Arctic to help place melt pond observations into context with regard to spatial scaling, regional differences, and relatability to model parameterizations.

In this study, we demonstrated the value of using MOSAiC observations to evaluate the realism of models in simulating the summer evolution of snow and melt ponds. Accurate model parameterizations of melt pond processes are a challenge due to limited understanding of melt pond processes and propagating uncertainties, such as those from snowfall and snow/ice melt. Through model-observation comparisons, we revealed possible weaknesses in specific model parameterizations that may have important consequences for accurately simulating albedo feedbacks. These include the distribution of meltwater across sea-ice thickness categories and the spatio-temporal changes in pond depth and areal coverage (**Figures 8c**, **8d**, and **12**). Our results point the way for further study of mechanisms driving pond formation and evolution and how those mechanisms may be better represented in models. Future efforts will build on the results presented here to enhance the treatment of melt pond processes in models, with the ultimate goal of improving simulated feedbacks and the predictive capability of climate models.

Data accessibility statement

- MOSAiC magnaprobe and GEM-2 data are archived in the MOSAiC Central Storage (MCS) and will be available at the time of final publication in the data repository PANGAEA under: Itkin, P., Webster, M., Hendricks, S., Oggier, M., Jaggi, M., Ricker, R., Arndt, S., Divine, D.V., von Albedyll, L., Raphael, I., Rohde, J., and G.E. Liston (2021): Magnaprobe snow and melt pond depth measurements from the 2019-2020 MOSAiC expedition. PANGAEA, https://doi.pangaea.de/10.1594/PANGAEA.937781 (dataset in review). Additional references to data sets that are already published are given in the bullets below.
- The gridded ALS data are archived on Zenodo under: Hutter, Nils, Hendricks, Stefan, Jutila, Arttu, Ricker, Robert, von Albedyll, Luisa, Birnbaum, Gerit, & Haas, Christian. (2021). Gridded airborne laser scanner (ALS) elevation data (L4) for three flights during MOSAiC (prerelease) (Version 1.0.0-alpha) [Data set]. Zenodo. http://doi.org/10.5281/zenodo.5121824.
- Ruler measurements of snow, subnivean pond, and melt pond depths from the albedo lines (Smith et al., 2021) are available at: https://arcticdata.io/catalog/view/doi%3A10.18739%2FA2ZG6G81T.
- Meteorological data were collected from MOSAiC from the Atmospheric Radiation Measurement (ARM) User Facility, a US Department of Energy Office of Science User Facility managed by the Biological and Environmental Research Program, under expedition number MOSAiC20192020 and project identifier AWI_PS122_00: Meteorological Measurements associated with the Surface Meteorological Instrumentation (PWD) and Aerosol Observing System (AOSMET). 2020-04-01 to 2020-09-30, ARM Mobile Facility (MOS) MOSAIC (Drifting Obs - Study of Arctic Climate); AMF2 (M1). Compiled by J. Kyrouac, S. Springston, and D. Holdridge. ARM Data Center. Data set accessed May 27, 2021, at http://dx.doi.org/10.5439/1025153.
- Drift track data are available at: Rex, Markus (2021): The master track of POLARSTERN cruise PS122/4 and PS122/5 in 1 sec resolution was used for drift correction. Alfred Wegener Institute, Helmholtz Centre for Polar and Marine Research, Bremerhaven, PANGAEA, https://doi.org/10.1594/PANGAEA.926830 and https://doi.org/10.1594/PANGAEA.926911.
- Melt pond data from the SHEBA field campaign are available in Perovich et al. (2002b; 2003).
- Melt pond data from the 2011 APLIS/ICEX drift in Webster et al. (2015) are available at: http://psc.apl.uw.edu/melt-pond-data.
- MIZMAS data (Zhang et al., 2018) are available at: https://pscfiles.apl.uw.edu/zhang/MIZMAS/.

- The CESM2 large ensemble data (https://doi.org/10.26024/kgmp-c556) are available at: https://www.earthsystemgrid.org/dataset/ucar.cgd.cesm2le.output.html.
- The OSSP-derived satellite pond fractions (Wright et al., 2020) for MOSAiC are available at the Arctic Data Center under: Wright, N., Webster, M., and C. Polashenski. (2021). Melt Pond Maps around the Multidisciplinary drifting Observatory for the Study of Arctic Climate (MOSAiC) Drifting Station derived from High Resolution Optical Imagery, 2020. urn: node: ARCTIC. doi:10.18739/A2696ZZ9W.
- SkySat Imagery is courtesy of Planet Labs, Inc.
- Raw and preprocessed image data from DigitalGlobe WorldView images can be acquired from DigitalGlobe or the Polar Geospatial Center at the University of Minnesota. Geospatial support for this work was provided by the Polar Geospatial Center under NSF-OPP awards 1043681 and 1559691, and the imagery was provided through the DigitalGlobe NextView License (2020).
- Sea-ice concentration data (Spreen et al., 2008) in **Figure 1** are available from the University of Bremen at: https://seaice.uni-bremen.de/sea-ice-concentration/amsre-amsr2/.

Supplemental files

The supplemental files for this article can be found as follows:

Figures S1–S4. Table S1. Docx

Acknowledgments

Data used in this article were produced as part of the international MOSAiC project with the tag MOSAiC20192020 and the Project_ID: AWI_PS122_00. We thank all people involved in the expedition of the R/V *Polarstern* during MOSAiC in 2019–2020 as listed in Nixdorf et al. (2021). For the CESM simulations, we acknowledge computing and data storage resources, including the Cheyenne supercomputer (doi:10.5065/D6RX99HX), which were provided by the Computational and Information Systems Laboratory (CISL) at NCAR. NCAR is sponsored by the National Science Foundation. We are especially grateful for the assistance of James S. Hak from the United States Geological Survey, and Mike Cloutier and Paul Morin from the University of Minnesota Polar Geospatial Center in acquiring WorldView imagery. WorldView satellite imagery was provided with the DigitalGlobe NextView License (2020) through the University of Minnesota Polar Geospatial Center. We are grateful for data collection assistance from: Zoe Brasseur, Ulrike Dietrich, Dmitry Divine, Alberto Enriquez, Allison Fong, Celia Gelfman, Marlene Goering, Antonia Immerz, Harold Jager, Tuija Jokinen, Benjamin Lange, Amy MacFarlane, Marcel Nicolaus, Julia Regnery, Jan Rohde, Evgenii Salganik, Katrin Schmidt, Katyanne Shoemaker, Matthew Shupe, Gunnar Spreen, Aikaterini Tavri, Linda Thielke, Juarez Viegas, the MOSAiC logistic team, and crew of the *Polarstern*. We thank David Bailey for his assistance in running the CESM2 large ensemble members, and Marcel Nicolaus and Stephen Warren for providing helpful comments in preparing this manuscript. We thank Jody Deming, Walt Meier, and an anonymous reviewer for their time and constructive reviews.

Funding

MAW conducted this work under the National Aeronautics and Space Administration's New Investigator Program in Earth Science (80NSSC20K0658). DKP and IAR conducted this work under the National Science Foundation Project 1724540. JZ was supported by the NASA Cryosphere Program (NNX17AD27G and 80NSSC20K1253) and the NSF Office of Polar Programs (PLR-1603259). MMH acknowledges funding from NSF OPP-1724748. BL conducted this work under the NSF OPP-1724467. MMS was supported by NSF OPP-1724467 and OPP-1724748. NH and ALS data processing were supported by the BMBF IceSense (03F0866A) project. FL was supported by the BMWi project ArcticSense (50EE1917A) and by Prof. Dr. Werner Petersen-Stiftung. LvA was funded by the AWI through the project AWI_ICE.

Competing interests

The authors declare that they have no competing interests.

Author contributions

Contributed to the conception and design: SH, MMH, PI, DKP, MAW.

Contributed to the acquisition of data: SH, MMH, NH, PI, FL, DKP, IR, MS, LvA, MAW, NW, JZ.

Contributed to analysis and interpretation of data: SH, MMH, NH, PI, FL, DKP, IR, LvA, MAW, NW, JZ.

Drafted and/or revised the article: All authors.

Approved the submitted version for publication: All authors.

References

Anhaus, P, **Katlein, C**, **Nicolaus, M**, **Hoppmann, M**, **Haas, C**. 2021. From bright windows to dark spots: Snow cover controls melt pond optical properties during refreezing. *Geophysical Research Letters* **48**(23): e2021GL095369. DOI: http://dx.doi.org/10.1002/essoar.10507628.2.

Bailey, DA, Holland, MM, DuVivier, AK, Hunke, EC, Turner, AK. 2020. Impact of a new sea ice thermodynamic formulation in the CESM2 sea ice component. *Journal of Advances in Modeling Earth Systems* **12**: e2020MS002154. DOI: http://dx.doi.org/10.1029/2020MS002154.

Brandt, RE, **Warren, SG**, **Worby, AP**, **Grenfell, TC**. 2005. Surface albedo of the Antarctic sea-ice zone. *Journal of Climate* **18**: 3606–3622. DOI: http://dx.doi.org/10.1175/JCLI3489.1.

Buckley, EM, **Farrell, SL**, **Duncan, K**, **Connor, LN**, **Kuhn, JM**, **Dominguez, RT**. 2020. Classification of sea ice summer melt features in high-resolution IceBridge imagery. *Journal of Geophysical Research:*

Oceans **125**. DOI: http://dx.doi.org/10.1029/2019JC015738.

Danabasoglu, G, **Lamarque, JF**, **Bachmeister, J**, **Bailey, DA**, **DuVivier, AK**, **Edwards, J**, **Emmons, LK**, **Fasullo, J**, **Garcia, R**, **Gettelman, A**, **Hannay, C**, **Holland, MM**, **Large, WG**, **Lauritzen, PH**, **Lawrence, DM**, **Lenaerts, JTM**, **Lindsay, K**, **Lipscomb, WH**, **Mills, MJ**, **Neale, R**, **Oleson, KW**, **Otto-Bliesner, B**, **Phillips, AS**, **Sacks, W**, **Tilmes, S**, **van Kampenhout, L**, **Vertenstein, M**, **Bertini, A**, **Dennis, J**, **Deser, C**, **Fischer, C**, **Fox-Kemper, B**, **Kay, JE**, **Kinnison, D**, **Kushner, PJ**, **Larson, VE**, **Long, MC**, **Mickelson, S**, **Moore, JK**, **Nienhouse, E**, **Polvani, L**, **Rasch, PJ**, **Strand, WG**. 2020. The Community Earth System Model Version 2 (CESM2). *Journal of Advances in Modeling Earth Systems* **12**. DOI: http://dx.doi.org/10.1029/2019MS001916.

DeRepentigny, P, **Jahn, A**, **Holland, MM**, **Smith, A**. 2020. Arctic sea ice in the two Community Earth System Model version 2 (CESM2) configurations during the 20th and 21st centuries. *Journal of Geophysical Research: Oceans* **125**: e2020JC016133. DOI: http://dx.doi.org/10.1029/2020JC016133.

DuVivier, AK, **Holland, MM**, **Kay, JE**, **Tilmes, S**, **Gettelman, A**, **Bailey, D**. 2020. Arctic and Antarctic sea ice state in the Community Earth System Model Version 2. *Journal of Geophysical Research: Oceans* **125**: e2019JC015934. DOI: http://dx.doi.org/10.1029/2019JC015934.

Eicken, H, **Grenfell, TC**, **Perovich, DK**, **Richter-Menge, JA**, **Frey, K**. 2004. Hydraulic controls of summer Arctic pack ice albedo. *Journal of Geophysical Research* **109**: C08007. DOI: http://dx.doi.org/10.1029/2003JC001989.

Eicken, H, **Krouse, HR**, **Kadko, D**, **Perovich, DK**. 2002. Tracer studies of pathways and rates of meltwater transport through Arctic summer sea ice. *Journal of Geophysical Research* **107**(C10): 8046. DOI: http://dx.doi.org/10.1029/2000JC000583.

Fetterer, F, **Untersteiner, N**. 1998. Observations of melt ponds on Arctic sea ice. *Journal of Geophysical Research* **103**(C11): 24,821–24,835. DOI: http://dx.doi.org/10.1029/98JC02034.

Flocco, D, **Feltham, DL**. 2007. A continuum model of melt pond evolution on Arctic sea ice. *Journal of Geophysical Research* **112**: C08016. DOI: http://dx.doi.org/10.1029/2006JC003836.

Flocco, D, **Feltham, DL**, **Turner, AK**. 2010. Incorporation of a physically based melt pond scheme into the sea ice component of a climate model. *Journal of Geophysical Research* **115**: C08012. DOI: http://dx.doi.org/10.1029/2009JC005568.

Flocco, D, **Schroeder, D**, **Feltham, DL**, **Hunke, EC**. 2012. Impact of melt ponds on Arctic sea ice simulations from 1990 to 2007. *Journal of Geophysical Research* **117**: C09032. DOI: http://dx.doi.org/10.1029/2012JC008195.

Gardner, J, **Richter-Menge, J**, **Farrell, S**, **Brozena, J**. 2012. Coincident multiscale estimates of Arctic sea ice thickness. *Eos Transactions AGU* **93**(6): 57–58. DOI: http://dx.doi.org/10.1029/2012EO060001.

Hibler, WD, III. 1980. Modeling a variable thickness sea ice cover. *Monthly Weather Review* **1**: 943–1973. DOI: http://dx.doi.org/10.1175/1520-0493(1980)108<1943:MAVTSI>2.0.CO;2.

Holland, MM, **Bailey, DA**, **Briegleb, BP**, **Light, B**, **Hunke, E**. 2012. Improved sea ice shortwave radiation physics in CCSM4: The impact of melt ponds and aerosols on arctic sea ice. *Journal of Climate* **25**: 1413–1430. DOI: http://dx.doi.org/10.1175/JCLI-D-11-00078.1.

Hunke, EC, Dukowicz, JK. 2002. The elastic-viscous-plastic sea ice dynamics model in general orthogonal curvilinear coordinates on a sphere–incorporation of metric terms. *Monthly Weather Review* **130**: 1848–1865. DOI: http://dx.doi.org/10.1175/1520-0493(2002)130<1848:TEVPSI>2.0.CO;2.

Hunke, EC, **Hebert, DA**, **Lecomte, O**. 2013. Level-ice melt ponds in the Los Alamos sea ice model, CICE. *Ocean Modelling* **71**: 26–42. DOI: http://dx.doi.org/10.1016/j.ocemod.2012.11.008.

Hunke, EC, **Lipscomb, WH**, **Turner, AK**, **Jeery, N**, **Elliot, S**. 2015. CICE: The Los Alamos Sea ice model documentation and software user's manual version 5.1. Los Alamos National Laboratory. Tech. Rep. No. LA-CC-06-012.

Hunkeler, PA, **Hendricks, S**, **Hoppmann, M**, **Farquharson, CG**, **Kalscheuer, T**, **Grab, M**, **Kaufmann, MS**. 2016. Improved 1D inversions for sea ice thickness and conductivity from electromagnetic induction data: Inclusion of nonlinearities caused by passive bucking. *Geophysics* **81**(1): Wa45–Wa58. DOI: http://dx.doi.org/10.1190/Geo2015-0130.1.

Hutter, N, **Hendricks, S**, **Jutila, A**, **Ricker, R**, **von Albedyll, L**, **Birnbaum, G**, **Haas, C**. 2021. Gridded airborne laser scanner (ALS) elevation data (L4) for three flights during MOSAiC (prerelease) (Version 1.0.0-alpha) [dataset]. *Zenodo*. DOI: http://dx.doi.org/10.5281/zenodo.5121824.

Katlein, C, **Arndt, S**, **Belter, HJ**, **Castellani, G**, **Nicolaus, M**. 2019. Seasonal evolution of light transmission distributions through Arctic sea ice. *Journal of Geophysical Research: Oceans* **124**: 5418–5435. DOI: http://dx.doi.org/10.1029/2018JC014833.

Kay, JE, **DeRepentigny, P**, **Holland, MM**, **Bailey, DA**, **DuVivier, AK**, **Blanchard-Wrigglesworth, E**, **Deser, C**, **Jahn, A**, **Singh, HA**, **Smith, MM**, **Webster, MA**, **Edwards, J**, **Lee, S**, **Rodgers, K**, **Rosenbloom, NA**. 2022. Less surface sea ice melt in the CESM2 improves Arctic sea ice simulation with minimal non-polar climate impacts. *Journal of Advances in Modeling Earth Systems*. DOI: http://dx.doi.org/10.1002/essoar.10507477.1.

Light, B, **Dickinson, S**, **Perovich, DK**, **Holland, MM**. 2015. Evolution of summer Arctic sea ice albedo in CCSM4 simulations: Episodic summer snowfall and frozen summers. *Journal of Geophysical Research: Oceans* **120**: 284–303. DOI: http://dx.doi.org/10.1002/2014JC010149.

Light, B, **Grenfell, TC**, **Perovich, DK**. 2008. Transmission and absorption of solar radiation by Arctic sea ice during the melt season. *Journal of Geophysical Research* **113**: C03023. DOI: http://dx.doi.org/10.1029/2006JC003977.

Light, B, **Smith, MM**, **Perovich, DK**, **Webster, M**, **Holland, M**, **Linhardt, F**, **Raphael, IA**, **Clemens-Sewall, D**, **MacFarlane, A**, **Anhaus, P**, **Bailey, D**. n.d. Arctic sea ice albedo: Spectral composition, spatial heterogeneity, and temporal evolution observed during the MOSAiC drift. *Elementa: Science of the Anthropocene*, in press.

Lüthje, M, **Feltham, DL**, **Taylor, PD**, **Worster, MG**. 2006. Modeling the summertime evolution of sea-ice melt ponds. *Journal of Geophysical Research* **111**: C02001. DOI: http://dx.doi.org/10.1029/2004JC002818.

Massonnet, F, **Fichefet, T**, **Goosse, H**, **Bitz, CM**, **Philippon-Berthier, G**, **Holland, MM**, **Barriat, PY**. 2012. Constraining projections of summer Arctic sea ice. *The Cryosphere* **6**(6): 1383–1394. DOI: http://dx.doi.org/10.5194/tc-6-1383-2012.

Nicolaus, M, **Katlein, C**, **Maslanik, J**, **Hendricks, S**. 2012. Changes in Arctic sea ice result in increasing light transmittance and absorption. *Geophysical Research Letters* **39**: L24501. DOI: http://dx.doi.org/10.1029/2012GL053738.

Nicolaus, M, **Perovich, DK**, **Spreen, G**, **Granskog, MA**, **Albedyll, L von**, **Angelopoulos, M**, **Anhaus, P**, **Arndt, S**, **Belter, HJ**, **Bessonov, V**, **Birnbaum, G**, **Brauchle, J**, **Calmer, R**, **Cardellach, E**, **Cheng, B**, **Clemens-Sewall, D**, **Dadic, R**, **Damm, E**, **Boer, G de**, **Demir, O**, **Dethloff, K**, **Divine, DV**, **Fong, AA**, **Fons, S**, **Frey, MM**, **Fuchs, N**, **Gabarró, C**, **Gerland, S**, **Goessling, HF**, **Gradinger, R**, **Haapala, J**, **Haas, C**, **Hamilton, J**, **Hannula, H-R**, **Hendricks, S**, **Herber, A**, **Heuzé, C**, **Hoppmann, M**, **Høyland, KV**, **Huntemann, M**, **Hutchings, JK**, **Hwang, B**, **Itkin, P**, **Jacobi, H-W**, **Jaggi, M**, **Jutila, A**, **Kaleschke, L**, **Katlein, C**, **Kolabutin, N**, **Krampe, D**, **Kristensen, SS**, **Krumpen, T**, **Kurtz, N**, **Lampert, A**, **Lange, BA**, **Lei, R**, **Light, B**, **Linhardt, F**, **Liston, GE**, **Loose, B**, **Macfarlane, AR**, **Mahmud, M**, **Matero, IO**, **Maus, S**, **Morgenstern, A**, **Naderpour, R**, **Nandan, V**, **Niubom, A**, **Oggier, M**, **Oppelt, N**, **Pätzold, F**, **Perron, C**, **Petrovsky, T**, **Pirazzini, R**, **Polashenski, C**, **Rabe, B**, **Raphael, IA**, **Regnery, J**, **Rex, M**, **Ricker, R**, **Riemann-Campe, K**, **Rinke, A**, **Rohde, J**, **Salganik, E**, **Scharien, RK**, **Schiller, M**, **Schneebeli, M**, **Semmling, M**, **Shimanchuk, E**, **Shupe, MD**, **Smith, MM**, **Smolyanitsky, V**, **Sokolov, V**, **Stanton, T**, **Stroeve, J**, **Thielke, L**, **Timofeeva, A**, **Tonboe, RT**, **Tavri, A**, **Tsamados, M**, **Wagner, DN**, **Watkins, D**, **Webster, M**, **Wendisch, M**. 2022. Overview of the MOSAiC expedition: Snow and sea ice. *Elementa: Science of the Anthropocene*. DOI: http://dx.doi.org/10.1525/elementa.2021.000046.

Nixdorf, U, **Dethloff, K**, **Rex, M**, **Shupe, M**, **Sommerfeld, A**, **Perovich, DK**, **Nicolaus, M**, **Heuzé, C**, **Rabe, B**, **Loose, B**, **Damm, E**, **Gradinger, R**, **Fong, A**, **Maslowski, W**, **Rinke, A**, **Kwok, R**, **Spreen, G**, **Wendisch, M**, **Herber, A**, **Hirsekorn, M**, **Mohaupt, V**, **Frickenhaus, S**, **Immerz, A**, Weiss-**Tuider, K**, **König, B**, **Mengedoht, D**, **Regnery, J**, **Gerchow, P**, **Ransby, D**, **Krumpen, T**, **Morgenstern, A**, **Haas, C**. 2021. MOSAiC extended acknowledgement. *Zenodo*. DOI: http://dx.doi.org/10.5281/zenodo.5179738.

Notz, D, **Jahn, A**, **Holland, M**, **Hunke, E**, **Massonnet, F**, **Stroeve, J**, **Tremblay, B**, **Vancoppenolle, M**. 2016. The CMIP6 Sea-Ice Model Intercomparison Project (SIMIP): Understanding sea ice through climate-model simulations. *Geoscientific Model Development* **9**(9): 3427–3446. DOI: http://dx.doi.org/10.5194/gmd-9-3427-2016.

Perovich, DK. 2007. Light reflection and transmission by a temperate snow cover. *Journal of Glaciology* **53**(181): 201–210. DOI: http://dx.doi.org/10.3189/172756507782202919.

Perovich, DK, **Grenfell, TC**, **Light, B**, **Hobbs, PV**. 2002a. Seasonal evolution of the albedo of multiyear Arctic sea ice. *Journal of Geophysical Research* **107**(C10): 8044. DOI: http://dx.doi.org/10.1029/2000JC000438.

Perovich, DK, **Grenfell, TC**, **Richter-Menge, JA**, **Light, B**, **Tucker, III, WB**, **Eicken, H**. 2003. Thin and thinner: Sea ice mass balance measurements during SHEBA. *Journal of Geophysical Research* **108**(C3): 8050. DOI: http://dx.doi.org/10.1029/2001JC001079.

Perovich, DK, **Polashenski, C**. 2012. Albedo evolution of seasonal Arctic sea ice. *Geophysical Research Letters* **39**: L08501. DOI: http://dx.doi.org/10.1029/2012GL051432.

Perovich, DK, **Tucker, WB, III**, **Ligett, KA**. 2002b. Aerial observations of the evolution of ice surface conditions during summer. *Journal of Geophysical Research* **107**(C10): 8048. DOI: http://dx.doi.org/10.1029/2000JC000449.

Petrich, C, **Eicken, H**, **Polashenski, CM**, **Sturm, M**, **Harbeck, JP**, **Perovich, DK**, **Finnegan, DC**. 2012. Snow dunes: A controlling factor of melt pond distribution on Arctic sea ice. *Journal of Geophysical Research* **117**: C09029. DOI: http://dx.doi.org/10.1029/2012JC008192.

Polashenski, C, **Perovich, DK**, **Courville, Z**. 2012. The mechanisms of sea ice melt pond formation and evolution. *Journal of Geophysical Research* **117**: C01001. DOI: http://dx.doi.org/10.1029/2011JC007231.

Popović, P, **Abbot, D**. 2017. A simple model for the evolution of melt pond coverage on permeable Arctic sea ice. *The Cryosphere* **11**: 1149–1172. DOI: http://dx.doi.org/10.5194/tc-11-1149-2017.

Rodgers, KB, Lee, S-S, Rosenbloom, N, Timmermann, A, Danabasoglu, G, Deser, C, Edwards, J, Kim, J-E, Simpson, IR, Stein, K, Stuecker, MF, Yamaguchi, R, Bódai, T, Chung, E-S, Huang, L, Kim, WM, Lamarque, J-F, Lombardozzi, DL, Wieder, WR, Yeager, SG. 2021. Ubiquity of human-induced changes in climate variability. *Earth System*

Dynamics **12**: 1393–1411. DOI: http://dx.doi.org/10.5194/esd-12-1393-2021.

Rinke, A, Cassano, JJ, Cassano, EN, Jaiser, R, Handorf, D. 2021. Meteorological conditions during the MOSAiC expedition: Normal or anomalous? *Elementa: Science of the Anthropocene* **9**: 1. DOI: http://dx.doi.org/10.1525/elementa.2021.00023.

Rösel, A, **Kaleschke, L**, **Birnbaum, G**. 2012. Melt ponds on Arctic sea ice determined from MODIS satellite data using an artificial neural network. *Cryosphere* **6**(2): 431–446. DOI: http://dx.doi.org/10.5194/tc-6-431-2012.

Saha, S, **Moorthi, S**, **Wu, X**, **Wang, J**, **Nadiga, S**, **Tripp, P**, **Behringer, D**, **Hou, Y-T**, **Chuang, H**, **Iredell, M**, **Ek, M**, **Meng, J**, **Yang, R**, **Mendez, MP**, **Dool, H van den**, **Zhang, Q**, **Wang, W**, **Chen, M**, **Becker, E**. 2014. The NCEP climate forecast system version 2. *Journal of Climate* **27**(6): 2185–2208. DOI: http://dx.doi.org/10.1175/JCLI-D-12-00823.1.

Schröder, D, **Feltham, D**, **Flocco, D**, **Tsamados, M**. 2014. September Arctic sea-ice minimum predicted by spring melt-pond fraction. *Nature Climate Change* **4**: 353–357. DOI: http://dx.doi.org/10.1038/nclimate2203.

Scott, F, **Feltham, DL**. 2010. A model of the three-dimensional evolution of Arctic melt ponds on first-year and multiyear sea ice. *Journal of Geophysical Research* **115**: C12064. DOI: http://dx.doi.org/10.1029/2010JC006156.

Shepard, MK, **Campbell, BA**, **Bulmer, MH**, **Farr, TG**, **Gaddis, LR**, **Plaut, JJ**. 2001. The roughness of natural terrain: a planetary and remote sensing perspective. *Journal of Geophysical Research* **106**(E12): 32,777–32,795. DOI: http://dx.doi.org/10.1029/2000JE001429.

Shupe, M, **Rex, M**, **Blomquist, B**, **Persson, POG**, **Schmale, J**, **Uttal, T**, **Althausen, D**, **Angot, H**, **Archer, S**, **Bariteau, L**, **Beck, I**, **Bilberry, J**, **Bucci, S**, **Buck, C**, **Boyer, M**, **Brasseur, Z**, **Brooks, IM**, **Calmer, R**, **Cassano, J**, **Castro, V**, **Chu, D**, **Costa, D**, **Cox, CJ**, **Creamean, J**, **Crewell, S**, **Dahlke, S**, **Damm, E**, **Boer, G de**, **Deckelmann, H**, **Dethloff, K**, **Dütsch, M**, **Ebell, K**, **Ehrlich, A**, **Ellis, J**, **Engelmann, R**, **Fong, AA**, **Frey, MM**, **Gallagher, MR**, **Ganzeveld, L**, **Gradinger, R**, **Graeser, J**, **Greenamyer, V**, **Griesche, H**, **Griffiths, S**, **Hamilton, J**, **Heinemann, G**, **Helmig, D**, **Herber, A**, **Heuzé, C**, **Hofer, J**, **Houchens, T**, **Howard, D**, **Inoue, J**, **Jacobi, H-W**, **Jaiser, R**, **Jokinen, T**, **Jourdan, O**, **Jozef, G**, **King, W**, **Kirchgaessner, A**, **Klingebiel, M**, **Krassovski, M**, **Krumpen, T**, **Lampert, A**, **Landing, W**, **Laurila, T**, **Lawrence, D**, **Lonardi, M**, **Loose, B**, **Lüpkes, C**, **Maahn, M**, **Macke, A**, **Maslowski, W**, **Marsay, C**, **Maturilli, M**, **Mech, M**, **Morris, S**, **Moser, M**, **Nicolaus, M**, **Ortega, P**, **Osborn, J**, **Pätzold, F**, **Perovich, DK**, **Petäjä, T**, **Pilz, C**, **Pirazzini, R**, **Posman, K**, **Powers, H**, **Pratt, KA**, **Preußer, A**, **Quéléver, L**, **Radenz, M**, **Rabe, B**, **Rinke, A**, **Sachs, T**, **Schulz, A**, **Siebert, H**, **Silva, T**, **Solomon, A**, **Sommerfeld, A**, **Spreen, G**, **Stephens, M**, **Stohl, A**, **Svensson, G**, **Uin, J**, **Viegas, J**, **Voigt, C**, **Gathen, Pvd**, **Wehner, B**, **Welker, JM**, **Wendisch, M**, **Werner, M**, **Xie, ZQ**, **Yue, F**. 2022. Overview of the MOSAiC expedition: Atmosphere. *Elementa: Science of the Anthropocene* **10**. DOI: http://dx.doi.org/10.1525/elementa.2021.00060.

Shupe, M, **Rex, M**, **Dethloff, K**, **Damm, E**, **Fong, AA**, **Gradinger, R**, **Heuze, C**, **Loose, B**, **Makarov, A**, **Maslowski, W**, **Nicolaus, M**, **Perovich, D**, **Rabe, B**, **Rinke, A**, **Sokolov, V**, **Sommerfeld, A**. 2020. The MOSAiC expedition: A year drifting with the Arctic sea ice. *Arctic Report Card*. DOI: http://dx.doi.org/10.25923/9g3v-xh92.

Skyllingstad, ED, **Shell, KM**, **Collins, L**, **Polashenski, C**. 2015. Simulation of the melt season using a resolved sea ice model with snow cover and melt ponds. *Journal of Geophysical Research: Oceans* **120**: 5194–5215. DOI: http://dx.doi.org/10.1002/2014JC010569.

Smith, A, **Jahn, A**. 2019. Definition differences and internal variability affect the simulated Arctic sea ice melt season. *The Cryosphere* **13**: 1–20. DOI: http://dx.doi.org/10.5194/tc-13-1-2019.

Smith, M, **Light, B**, **Perovich, D**, **Webster, M**, **Anhaus, P**,**Clemens-Sewall, D**, **Linhardt, F**, **MacFarlane, A**, **Raphael, I**, **Bozzato, D**, **Brasseur, Z**, **Dadic, R**, **Fons, S**, **Immerz, A**, **Hannula, H-R**, **Hutchings, J**, **Pätzold, F**, **Regnery, J**, **Pirazzini, R**, **Tavri, A**. 2021. Raw files for broadband and spectral albedo measurements of the sea ice surface during the Multidisciplinary drifting Observatory for the Study of Arctic Climate (MOSAiC) campaign in the Central Arctic Ocean, April–September 2020. Arctic Data Center. DOI: http://dx.doi.org/10.18739/A2ZG6G81T.

Smith, RD, **Dukowicz, JK**, **Malone, RC**. 1992. Parallel ocean general-circulation modeling. *Physica D* **60**(1–4): 38–61. DOI: http://dx.doi.org/10.1016/0167-2789(92)90225-C.

Spreen, G, **Kaleschke, L**, **Heygster, G**. 2008. Sea ice remote sensing using AMSR-E 89 GHz channels. *Journal of Geophysical Research* **113**: C02S03. DOI: http://dx.doi.org/10.1029/2005JC003384.

Stroeve, JC, **Kattsov, V**, **Barrett, A**, **Serreze, M**, **Pavlova, T**, **Holland, M**, **Meier, WN**. 2012. Trends in Arctic sea ice extent from CMIP5, CMIP3 and observations. *Geophysical Research Letters* **39**(16). DOI: http://dx.doi.org/10.1029/2012GL052676.

Sturm, M, **Holmgren, J**. 2018. An automatic snow depth probe for field validation campaigns. *Water Resources Research* **54**: 9695–9701. DOI: http://dx.doi.org/10.1029/2018WR023559.

Turner, AK, **Hunke, EC**. 2015. Impacts of a mushy-layer thermodynamic approach in global sea-ice simulations using the CICE sea ice model. *Journal of Geophysical Research: Oceans* **120**: 1253–1275. DOI: http://dx.doi.org/10.1002/2014JC010358.

Turner, AK, Hunke, ECC, Bitz, CM. 2013. Two modes of sea-ice gravity drainage: A parameterization for large-scale modeling. *Journal of Geophysical*

Research Oceans **118**: 2279–2294. DOI: http://dx.doi.org/10.1002/jgrc.20171.

U.S. Army Corps of Engineers. 2002. *Ice engineering*. EM 1110-2-1612. Available at https://www.publications.usace.army.mil/USACE-Publications/Engineer-Manuals/u43544q/313131302D322D31363132/. Accessed 2 May 2022.

Uttal, T, **Curry, JA**, **McPhee, MG**, **Perovich, DK**, **Moritz, RE**, **Maslanik, JA**, **Guest, PS**, **Stern, HL**, **Moore, JA**, **Turenne, R**, **Heiberg, A**, **Serreze, MC**, **Wylie, DP**, **Persson, OG**, **Paulson, CA**, **Halle, C**, **Morison, JH**, **Wheeler, PA**, **Makshtas, A**, **Welch, H**, **Shupe, MD**, **Intrieri, JM**, **Stamnes, K**, **Lindsey, RW**, **Pinkel, R**, **Pegau, WS**, **Stanton, TP**, **Grenfeld, TC**. 2002. Surface heat budget of the Arctic Ocean. *Bulletin of the American Meteorological Society* **83**(2): 255–275. DOI: http://dx.doi.org/10.1175/1520-0477(2002)083<0255:SHBOTA>2.3.CO;2.

Webster, MA, **DuVivier, AK**, **Holland, MM**, **Bailey, DA**. 2021. Snow on Arctic sea ice in a warming climate as simulated in CESM. *Journal of Geophysical Research: Oceans* **125**: e2020JC016308. DOI: http://dx.doi.org/10.1029/2020JC016308.

Webster, MA, **Rigor, IG**, **Perovich, DK**, **Richter-Menge, JA**, **Polashenski, CM**, **Light, B**. 2015. Seasonal evolution of melt ponds on Arctic sea ice. *Journal of Geophysical Research: Oceans* **120**: 5968–5982. DOI: http://dx.doi.org/10.1002/2015JC011030.

Webster, MA, **Rigor, IG**, **Wright, N**. 2022. Observing Arctic sea ice. *Oceanography* **35**. DOI: http://dx.doi.org/10.5670/oceanog.2022.115.

World Meteorological Organization. 1970. WMO sea-ice nomenclature. Terminology, codes and illustrated glossary. Edition 1970. Geneva, Secretariat of the World meteorological organization. Available at https://library.wmo.int/doc_num.php?explnum_id=4651. Accessed 2 May 2022.

Wright, N, **Polashenski, C**. 2018. Open-source algorithm for detecting sea ice surface features in high-resolution optical imagery. *The Cryosphere* **12**(4): 1307–1329. DOI: http://dx.doi.org/10.5194/tc-12-1307-2018.

Wright, N, **Polashenski, C**, **McMichael, S**, **Beyer, R**. 2020. Observations of sea ice melt from Operation IceBridge imagery. *The Cryosphere* **14**: 3523–3536. DOI: http://dx.doi.org/10.5194/tc-14-3523-2020.

Wright, NC, **Polashenski, CM**. 2020. How machine learning and high-resolution imagery can improve melt pond retrieval from MODIS over current spectral unmixing techniques. *Journal of Geophysical Research: Oceans* **125**: e2019JC015569. DOI: http://dx.doi.org/10.1029/2019JC015569.

Zhang, J, **Rothrock, DA**. 2003. Modeling global sea ice with a thickness and enthalpy distribution model in generalized curvilinear coordinates. *Monthly Weather Review* **131**(5): 681–697. DOI: http://dx.doi.org/10.1175/1520-0493(2003)131<0845:MGSIWA>2.0.CO;2.

Zhang, J, **Schweiger, A**, **Webster, M**, **Light, B**, **Steele, M**, **Ashjian, C**, **Campbell, R**, **Spitz, Y**. 2018. Melt pond conditions on declining Arctic sea ice over 1979–2016: Model development, validation, and results. *Journal of Geophysical Research: Oceans* **123**: 7983–8003. DOI: http://dx.doi.org/10.1029/2018JC014298.

How to cite this article: Webster, MA, Holland, M, Wright, NC, Hendricks, S, Hutter, N, Itkin, P, Light, B, Linhardt, F, Perovich, DK, Raphael, IA, Smith, MM, von Albedyll, L, Zhang, J. 2022. Spatiotemporal evolution of melt ponds on Arctic sea ice: MOSAiC observations and model results. *Elementa: Science of the Anthropocene* 10(1). DOI: https://doi.org/10.1525/elementa.2021.000072

Domain Editor-in-Chief: Jody W. Deming, University of Washington, Seattle, WA, USA

Guest Editor: Marcel Nicolaus, Alfred Wegener Institute, Bremerhaven, Germany

Knowledge Domain: Ocean Science

Part of an Elementa Special Feature: The Multidisciplinary Drifting Observatory for the Study of Arctic Climate (MOSAiC)

Published: May 11, 2022 **Accepted:** April 17, 2022 **Submitted:** September 3, 2021